An Induction Motor Model for Virtual Drive Simulation Systems

Tatjana Martinovski

School of Electrical Engineering

Thesis submitted for examination for the degree of Master of Science in Technology.
Espoo 18.12.2019

Supervisor

Prof. Anouar Belahcen

Advisors

M.Sc. (Tech.) Victor Mukherjee

M.Sc. (Tech.) Jarkko Lalu

Aalto University
School of Electrical
Engineering

Aalto University
School of Electrical Engineering

Aalto University, P.O. BOX 11000, 00076 AALTO
www.aalto.fi
Abstract of the master's thesis

Author Tatjana Martinovski

Title An Induction Motor Model for Virtual Drive Simulation Systems

Degree programme Automation and Electrical Engineering

Major Electrical Power and Energy Engineering **Code of major** ELEC3024

Supervisor Prof. Anouar Belahcen

Advisors M.Sc. (Tech.) Victor Mukherjee, M.Sc. (Tech.) Jarkko Lalu

Date 18.12.2019 **Number of pages** 58 **Language** English

Abstract

In order to improve the control strategies and in turn increase the efficiency of the system, it is necessary to use accurate machine models. Finite element method (FEM) based machine models are considered sufficiently accurate. However, they cannot run in real time due to their computational costs. Traditional analytical models containing only constant-valued parameters can run in real time; however, they cannot model the machine power losses accurately enough.

This thesis proposes an analytical induction motor model. The electromagnetic (EM) loss calculation has been improved compared to the previous models by separating the rotor iron loss from the stator no load iron loss, by modelling the stray load loss (SLL) in the stator iron and by considering the loss due to the skin effect in the rotor bars. In the case of the 45 kW test motor and compared to the FEM computations, the error in the total EM loss is less than 0.1 % in the no load condition, and less than 0.6 % for the rated loading. The proposed model is suitable for time-domain simulations and it can run in real time. Therefore, it can be integrated with an electric drive simulation, which can be used in a variety of applications. The model has been implemented in the MATLAB Simulink environment.

FEM-based program FC-SMEK was used for computing the machine losses and for validating the results. The nonlinear least squares data fitting method *lsqnonlin* was used for identifying the parameters of the proposed model.

Keywords Induction motor, modelling, power losses, iron loss, FEM

Preface

This thesis was written at ABB Drives in Helsinki during summer and autumn of 2019.

I would like to thank my instructor Victor Mukherjee for his guidance and support throughout this thesis project. I am grateful to Prof. Anouar Belahcen for invaluable discussions and advice. I also wish to thank my instructor Jarkko Lalu for all the useful comments and the opportunity to work on this topic.

Finally, a great thank you to all the friends who have made my studies at Aalto an amazing experience.

Otaniemi, 18.12.2019

Tatjana Martinovski

Contents

Symbols and abbreviations

Symbols

$\boldsymbol{A}$	magnetic vector potential
$\boldsymbol{B}$	magnetic flux strength
C_{ex}	excess loss coefficient
C_{Ft}	eddy-current coefficient
C_{Hy}	hysteresis coefficient
$\boldsymbol{D}$	electric flux density
$\boldsymbol{E}$	electric field strength
f	frequency
f_{r}	frequency of the rotor
f_{s}	frequency of the stator
$\boldsymbol{H}$	magnetic field strength
$\boldsymbol{i}_{\mathrm{m}}$	magnetising current
$\boldsymbol{i}_{\mathrm{r}}$	rotor current
$\boldsymbol{i}_{\mathrm{s}}$	stator current
$\boldsymbol{J}$	electric current density
k_{R}	resistance factor
L_{M}	transformed magnetising (mutual) inductance
L_{m}	magnetising (mutual) inductance
L_{r}	rotor inductance
L_{rl}	rotor leakage inductance
L_{s}	stator inductance
L_{sl}	stator leakage inductance
L_{σ}	total leakage inductance
p	number of pole pairs
P_{ex}	excess power loss
P_{Hy}	hysteresis power loss
P_{Fe}	total power loss in the core
P_{Ft}	eddy-current power loss
P_{in}	input power
P_{loss}	total power loss
P_{out}	output power
P_{res}	resistive power loss
$P_{\mathrm{res,r}}$	resistive power loss of the rotor cage
$P_{\mathrm{res,s}}$	resistive power loss of the stator winding
R_{AC}	AC resistance
R_{DC}	DC resistance
R_{R}	transformed resistance of the rotor winding
R_{r}	resistance of the rotor winding
R_{s}	resistance of the stator winding
s	slip
$\boldsymbol{u}_{\mathrm{r}}$	rotor voltage

$\boldsymbol{u}_\mathrm{s}$	stator voltage
W_Hy	energy loss due to hysteresis
γ	Γ-model transformation coefficient
ε	electric permittivity
η	efficiency
θ_m	rotor angle
μ	magnetic permeability
μ_0	permeability of air
μ_r	relative permeability
ρ	electric charge density
σ	conductivity
$\boldsymbol{\psi}_\mathrm{r}$	rotor flux
$\boldsymbol{\psi}_\mathrm{s}$	stator flux
$\boldsymbol{\psi}_\mathrm{ag}$	air-gap flux
ω_M	mechanical angular speed of the rotor
ω_m	electrical angular speed of the rotor
ω_r	angular slip frequency
ω_s	electrical angular frequency of the stator

Operators

j	imaginary unit
$\nabla\times$	curl operator
$\nabla\cdot$	divergence operator
$\dfrac{\mathrm{d}}{\mathrm{d}t}$	derivative with respect to t
$\dfrac{\partial}{\partial t}$	partial derivative with respect to t
$\displaystyle\int_S$	integral over an open surface S
$\displaystyle\oint_s$	integral over a contour s

Abbreviations

2D	two-dimensional
3D	three-dimensional
AC	alternating current
DC	direct current
EM	electromagnetic
FEA	finite element analysis
FEM	finite element method
IM	induction machine
PWM	pulse width modulation
SLL	stray load loss

1 Introduction

1.1 Background and objectives

Over the past decades, induction machines have seen increasing usage in various applications, due to their robustness, price and versatility. However, efficiency and operational costs can be further improved through the use of electric drives and various control strategies. The control strategies can be improved with an accurate machine model. Additionally, accurate machine models may help to determine more accurate control parameters. Electrical machine models which are based on the finite element method (FEM) are sufficiently accurate. However, even the powerful computers available today cannot run FEM-based models in real time. As a result, such models are usually not suitable for control purposes due to their computational costs.

Traditionally, induction machines have been modelled for control purposes using the T-model [1]. The basic T-model consists of five constant-valued parameters: two resistance and three inductance machine-specific parameters. Even though this type of model is fairly simple and easy to implement, it is not always convenient for control purposes. Moreover, loading the machine increases the temperature, which then causes an increase in resistances. Additionally, the basic T-model cannot represent changes in inductances resulting from variations in flux magnitude. Naturally, neither of these fluctuations are included in a model with constant-valued parameters. Moreover, the basic T-model altogether ignores iron (or core) losses of the machine and takes into account only the resistive losses.

A number of studies have been conducted with the aim of including iron losses in the analytical model of an induction machine. A simple approach for including iron losses was proposed in [2]. This paper suggested modelling the iron losses with a constant iron resistance and an iron inductance. Another improvement to the conventional T-model was proposed in [3]. This study proposed a simple approach to implement the variation in inductance due to magnetic saturation. In addition, complicated control strategies can be simplified using a basic Γ or an inverse-Γ model instead of a T-model [1], [4]. Both of these types of models are more suitable for designing control algorithms. In addition to using a Γ-model, [5] proposed replacing the constant-valued resistance with a variable resistance. This allows the simulation of phenomena contributing to iron losses and hence improves the accuracy of the iron loss calculation [5]. Apart from an improved iron loss calculation, the model proposed in [5] also accounts for the variation in inductance due to magnetic saturation. Furthermore, as it is a Γ-model of an induction motor, the implementation into a control system is simple. However, estimating the iron losses of a loaded motor has not been investigated using this particular model.

The aim of this thesis is to design a model for an induction motor which is able to run in real time and to accurately calculate the electromagnetic losses of the machine. In order to achieve this, existing models from the literature will be analysed to establish the state of the research on this topic. Following this, the model proposed in [5] will be extended to a more accurate model from the electromagnetic

loss calculation perspective. To achieve the objective, data fitting will be performed from the results of various FEM analysis to identify different parameters of the improved model. Finally, the proposed computational model will be validated using FEM by comparing the simulation results at various operational points. The final contribution of the thesis will be the development of the improved induction motor model in MATLAB Simulink environment, which can be used in an electric drive simulation for a variety of applications.

1.2 Outline of the thesis

The rest of this thesis is organised as follows. Chapter 2 reviews the literature on induction machines, models and phenomena relevant to the power loss calculations. Chapter 3 describes the methods used for designing and verifying the model. Chapter 4 presents the proposed model and the comparison of the simulation and FEM results. Finally, Chapter 5 discusses the conclusions and possible future work.

2 Background

In order to successfully design an induction motor model, it is first necessary to understand the operating principles of such machine. The existing types of models need to be analysed to select the most suitable one. In addition, the previously developed equations for implementing a satisfactory power loss computation have to be studied. Therefore, this chapter briefly presents the theory underlying induction motors, starting with a brief description of the construction and working principles of induction motors in Section 2.1, proceeding thereafter with the common T-model and its transformation to the Γ-model in Section 2.2. Section 2.3 reports different components of the power losses in an induction machine, with a focus on iron losses. The section analyses the traditional approaches for modelling the losses as well as the results of recent research. Finally, Section 2.4 investigates magnetic saturation and explores the approaches for modelling this phenomenon.

2.1 Induction motor

Electrical machines are devices which convert electrical energy into mechanical and vice versa. Based on the type of current that an electrical machine operates with (direct – DC or alternating – AC), it can be classified as either a DC machine or an AC machine. DC machines require regular and thorough maintenance. In addition, they typically have lower efficiency than AC machines. Therefore, AC machines are of more significant research interest. The AC machines are further divided into synchronous and induction (or asynchronous) machines. Synchronous machines operate at a constant speed regardless of load, while the rotational speed of induction machines decreases as the load increases. Both synchronous and induction machines can be used as generators or as motors. Generators convert mechanical energy into electrical energy, while motors convert electrical energy into mechanical energy. The most common usage for an induction machine is as a motor in industrial applications. Even though its efficiency is typically lower than that of a synchronous motor, an induction motor is a popular choice due to its durability, robustness and price.

An induction motor comprises a stationary part (stator) and a rotational part (rotor). Induction motors are typically magnetised from the stator, which normally has a three-phase winding. The currents in the stator windings induce the magnetic field that rotates with the synchronous angular frequency ω_s. Some of the induction motors have a three-phase winding on the rotor side as well, connected in a similar way as the stator winding. Such a machine (as the doubly-fed induction motor studied in [6]) is called a wound rotor induction motor. However, an induction motor most commonly has a squirrel-cage rotor. As the focus of this thesis is on such machine type, wound rotor machines are not discussed further. As long as the motor is not loaded mechanically, the rotor and the magnetic field rotate synchronously, thus inducing no current in the rotor from the synchronous flux of the stator. Once the motor is loaded, the rotor angular speed starts lagging behind the synchronous flux by the angular slip frequency. This then induces the current in the rotor winding, which in turn produces electromagnetic torque. If the electrical angular speeds of

the stator supply and the rotor are respectively ω_s and ω_m, slip is defined as [4]

$$s = \frac{\omega_\mathrm{s} - \omega_\mathrm{m}}{\omega_\mathrm{s}}. \tag{2.1}$$

Angular slip frequency can then be defined as

$$\omega_\mathrm{r} = s\omega_\mathrm{s} = \omega_\mathrm{s} - \omega_\mathrm{m}. \tag{2.2}$$

This notation will henceforth be used in the rest of the thesis. It is important to note that the stator winding can have more than one pole-pair. The number of pole-pairs is typically expressed as p, and when $p > 1$, mechanical angular speed does not equal to the electrical angular speed of the rotor. Instead, mechanical angular speed is calculated as the ratio of the electrical angular speed and the number of pole pairs:

$$\omega_\mathrm{M} = \frac{\omega_\mathrm{m}}{p}. \tag{2.3}$$

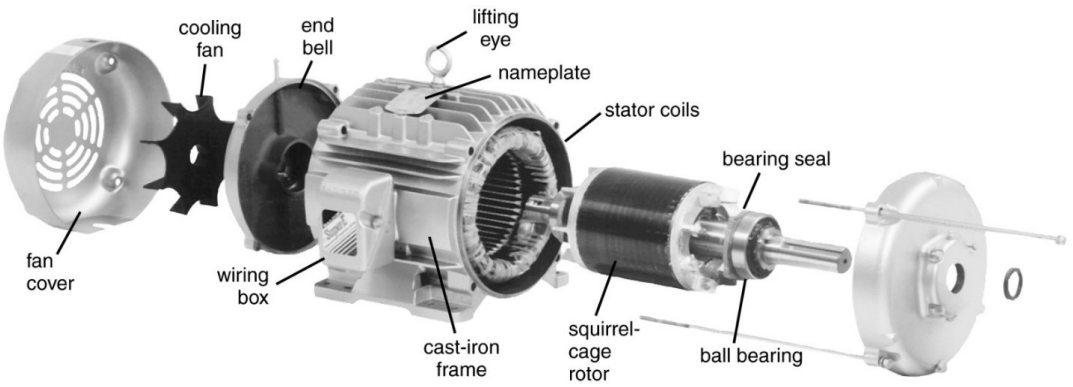

Figure 1: Construction of a squirrel-cage induction motor [7]

Construction of a totally closed fan-cooled squirrel-cage induction motor is shown in Fig. 1. The cast-iron frame protects the insides of the motor and prevents the exchange of air between inside and outside of the motor. The fan is located outside of the motor and it causes air circulation to cool down the motor. The stator is placed inside the motor frame, and consists of laminated iron core and windings made of copper. Stator windings are situated inside the stator slots, as can be seen in Fig. 2. The rotor is placed inside the stator. The rotor is made up from a stack of steel laminations. Molten aluminium is forced into the rotor slots in order to form the so-called squirrel cage winding. Aluminium bars are short-circuited together, forming end-rings. The shape of the rotor cage resembles a squirrel or a hamster cage, hence the name. Rotor slots are normally skewed. This results in decrease in torque ripple. In addition, skewing the rotor slots leads to a decrease in iron losses [8]. In order to rotate, the rotor typically needs to be supported by bearings that are placed on each side of the shaft.

The air gap between the stator and the rotor is typically very narrow. In the induction motors with the rated power of 100 kW or less, the air-gap is less than

1 mm wide [4]. The wider the air gap, the smaller the mutual inductance, which means that large stator magnetising current is required to produce the needed rotor flux. High magnetising current results in increased losses in the stator winding, which further causes the decrease in overall efficiency of the machine and increase in temperature. For this reason, it is important to design the induction motor so that the width of the air gap is small. However, a small air gap may lead to an increase in eddy-current losses as well as the surface losses in the rotor [9]. Therefore, there is no optimal air-gap length, instead it is defined empirically [9].

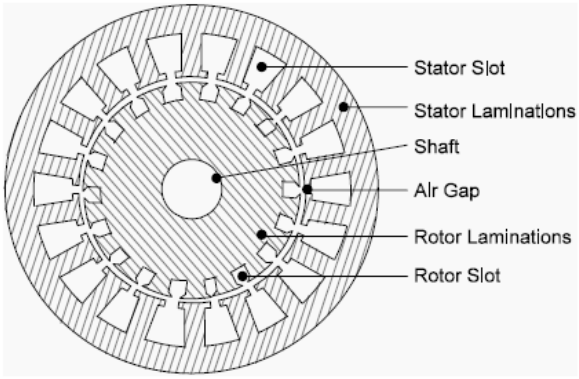

Figure 2: Cross-sectional view of an induction motor [10]

It is worth mentioning that not all induction motors are constructed exactly as the one depicted in Fig. 1. For example, some do not have a built-in fan. Moreover, the enclosure of the motor might be different. Furthermore, induction motors for certain applications have an outer rotor, i.e. the stator is placed inside the rotor [11]. Some are also bearingless, such as the machine studied in [12]. Nonetheless, the operational principle is the same.

2.2 Modelling an induction motor

In this section, the traditional dynamic T-model of an induction motor and its equivalent circuit are first presented (Fig. 3). Then, simplification of the T-model into the Γ-model is explained and the relevant relations are provided. From then on, Γ-model and its parameters will be used throughout the thesis.

Variables are represented in the form of space vectors. For example, the space vector of the stator voltage can be derived from the phase voltages as [1]

$$\boldsymbol{u}_\mathrm{s} = \frac{2}{3}(u_\mathrm{a} + u_\mathrm{b}e^{\frac{2\pi}{3}} + u_\mathrm{c}e^{\frac{4\pi}{3}}). \tag{2.4}$$

Space vectors of the currents and flux linkages can be derived similarly from the phase currents and flux linkages, respectively. The transient analysis is performed in the complex number form, so in dq-coordinates stator voltage can be represented as

$$\boldsymbol{u}_\mathrm{s} = u_\mathrm{ds} + ju_\mathrm{qs}, \tag{2.5}$$

where j is the imaginary unit operator. Phase currents and flux linkages can be represented in the same manner. Bold symbols (such as $\boldsymbol{u}_\mathrm{s}$) indicate space vectors.

In the stator circuit, a part of the stator voltage is dissipated in the stator resistance, while the rest of the voltage builds up the flux in the stator winding. Therefore, it holds [4] that

$$\boldsymbol{u}_\mathrm{s}^\mathrm{s} = R_\mathrm{s}\boldsymbol{i}_\mathrm{s}^\mathrm{s} + \frac{\mathrm{d}\boldsymbol{\psi}_\mathrm{s}^\mathrm{s}}{\mathrm{d}t}, \tag{2.6}$$

where $\boldsymbol{u}_\mathrm{s}^\mathrm{s}$ is the stator voltage, R_s resistance of the stator winding, $\boldsymbol{i}_\mathrm{s}^\mathrm{s}$ stator current and $\boldsymbol{\psi}_\mathrm{s}^\mathrm{s}$ stator flux linkage. Superscript $^\mathrm{s}$ denotes space vectors in the stator coordinates and subscript $_\mathrm{s}$ refers to stator values. Rotor circuit can be considered equivalently:

$$\boldsymbol{u}_\mathrm{r}^\mathrm{r} = R_\mathrm{r}\boldsymbol{i}_\mathrm{r}^\mathrm{r} + \frac{\mathrm{d}\boldsymbol{\psi}_\mathrm{r}^\mathrm{r}}{\mathrm{d}t}, \tag{2.7}$$

where $\boldsymbol{u}_\mathrm{r}^\mathrm{r}$ is the rotor voltage, R_r resistance of the rotor winding, $\boldsymbol{i}_\mathrm{r}^\mathrm{r}$ rotor current and $\boldsymbol{\psi}_\mathrm{r}^\mathrm{r}$ rotor flux linkage. Superscript $^\mathrm{r}$ denotes space vectors in the rotor coordinates and subscript $_\mathrm{r}$ refers to rotor values. Since this thesis only considers a squirrel-cage motor, $\boldsymbol{u}_\mathrm{r}^\mathrm{r} = 0$ holds. In order to transform rotor equation into stator coordinates, rotor angle is determined as

$$\theta_\mathrm{m} = \int_0^t \omega_\mathrm{m}\mathrm{d}t, \tag{2.8}$$

where ω_m is the electrical angular speed of the rotor. Then, rotor current and the flux linkage in the stator reference frame are derived as follows, respectively

$$\boldsymbol{i}_\mathrm{r}^\mathrm{s} = e^{j\theta_\mathrm{m}}\boldsymbol{i}_\mathrm{r}^\mathrm{r}, \tag{2.9}$$

$$\boldsymbol{\psi}_\mathrm{r}^\mathrm{s} = e^{j\theta_\mathrm{m}}\boldsymbol{\psi}_\mathrm{r}^\mathrm{r}. \tag{2.10}$$

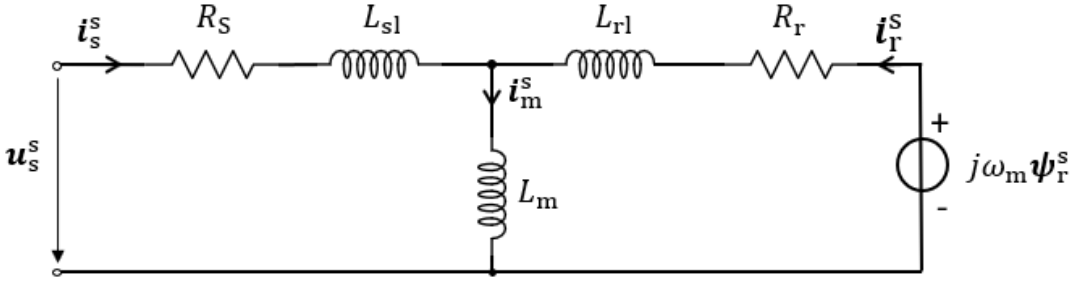

Figure 3: Dynamic T-equivalent circuit [4]

Therefore, considering equations 2.8, 2.9 and 2.10, equation 2.7 can be rewritten in stationary coordinates as

$$0 = -R_\mathrm{r}\boldsymbol{i}_\mathrm{r}^\mathrm{s} - \frac{\mathrm{d}\boldsymbol{\psi}_\mathrm{r}^\mathrm{s}}{\mathrm{d}t} + j\omega_\mathrm{m}\boldsymbol{\psi}_\mathrm{r}^\mathrm{s}. \tag{2.11}$$

Next, assuming linear magnetic conditions, the air-gap flux (in stator coordinates) can be shown as

$$\boldsymbol{\psi}_\mathrm{ag}^\mathrm{s} = L_\mathrm{m}\boldsymbol{i}_\mathrm{m}^\mathrm{s}, \tag{2.12}$$

where L_m is the magnetising (mutual) inductance between the stator and the rotor, and $\boldsymbol{i}_\mathrm{m}^\mathrm{s}$ is the magnetising current. Since the stator flux equals to the sum of the air-gap and the stator leakage flux, and equivalently for the rotor, it yields

$$\boldsymbol{\psi}_\mathrm{s}^\mathrm{s} = L_\mathrm{m}\boldsymbol{i}_\mathrm{m}^\mathrm{s} + L_\mathrm{sl}\boldsymbol{i}_\mathrm{s}^\mathrm{s}, \tag{2.13}$$

$$\boldsymbol{\psi}_\mathrm{r}^\mathrm{s} = L_\mathrm{m}\boldsymbol{i}_\mathrm{m}^\mathrm{s} + L_\mathrm{rl}\boldsymbol{i}_\mathrm{r}^\mathrm{s}, \tag{2.14}$$

where L_sl and L_rl are the stator and the rotor leakage inductances, respectively. The stator and the rotor inductances are then $L_\mathrm{s} = L_\mathrm{m} + L_\mathrm{sl}$ and $L_\mathrm{r} = L_\mathrm{m} + L_\mathrm{rl}$, respectively. Considering 2.13 and 2.14, Equations 2.6 and 2.7 can now be written as

$$\boldsymbol{u}_\mathrm{s}^\mathrm{s} = R_\mathrm{s}\boldsymbol{i}_\mathrm{s}^\mathrm{s} + L_\mathrm{sl}\frac{\mathrm{d}\boldsymbol{i}_\mathrm{s}^\mathrm{s}}{\mathrm{d}t} + L_\mathrm{m}\frac{\mathrm{d}\boldsymbol{i}_\mathrm{m}^\mathrm{s}}{\mathrm{d}t}, \tag{2.15}$$

$$0 = R_\mathrm{r}\boldsymbol{i}_\mathrm{r}^\mathrm{s} + L_\mathrm{rl}\frac{\mathrm{d}\boldsymbol{i}_\mathrm{r}^\mathrm{s}}{\mathrm{d}t} + L_\mathrm{m}\frac{\mathrm{d}\boldsymbol{i}_\mathrm{m}^\mathrm{s}}{\mathrm{d}t}. \tag{2.16}$$

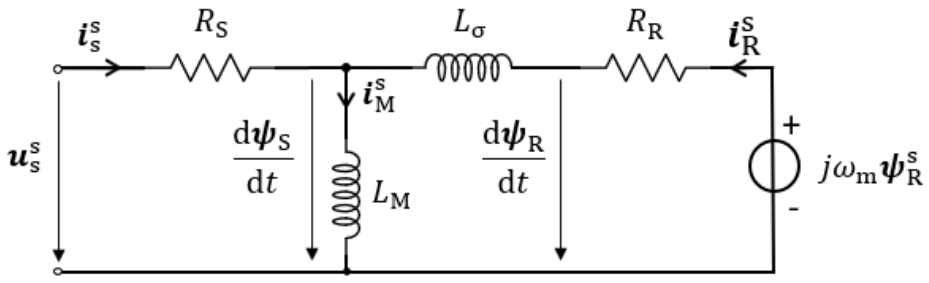

Figure 4: Dynamic Γ-equivalent circuit [1]

Even though the T model is dynamic, it can be easily simplified into the Γ-model (Fig. 4). Since the currents are linearly dependent: $\boldsymbol{i}_\mathrm{m}^\mathrm{s} = \boldsymbol{i}_\mathrm{s}^\mathrm{s} + \boldsymbol{i}_\mathrm{r}^\mathrm{s}$, the inductances can be modified so that only two instead of three are utilised in the model. New rotor variables are defined as [4]

$$\boldsymbol{\psi}_\mathrm{R}^\mathrm{s} = \gamma\boldsymbol{\psi}_\mathrm{r}^\mathrm{s} \tag{2.17}$$

and

$$\boldsymbol{i}_{\mathrm{R}}^{\mathrm{s}} = \frac{1}{\gamma}\boldsymbol{i}_{\mathrm{r}}^{\mathrm{s}}. \tag{2.18}$$

These definitions can be substituted into Equations 2.13 and 2.14, and if γ is chosen so that the stator and the rotor currents have equal coefficients, the leakage inductance gets referred to the rotor side. That transformation results in the Γ-model [1]. The parameter γ then becomes

$$\gamma = \frac{L_{\mathrm{s}}}{L_{\mathrm{m}}}. \tag{2.19}$$

Replacing the coefficients in Equations 2.13 and 2.14 with γ given in Equation 2.19, new parameters: the transformed magnetising inductance, the total leakage inductance and the transformed rotor resistance become, respectively

$$L_{\mathrm{M}} = \gamma L_{\mathrm{m}} = L_{\mathrm{s}}, \tag{2.20}$$

$$L_{\sigma} = \gamma L_{\mathrm{sl}} + \gamma^2 L_{\mathrm{rl}} = \frac{L_{\mathrm{sl}} + L_{\mathrm{M}}}{L_{\mathrm{M}}} L_{\mathrm{sl}} + \frac{(L_{\mathrm{sl}} + L_{\mathrm{M}})^2}{L_{\mathrm{M}}^2} L_{\mathrm{rl}} \approx L_{\mathrm{sl}} + L_{\mathrm{rl}}, \tag{2.21}$$

$$R_{\mathrm{R}} = \gamma^2 R_{\mathrm{r}} = \left(\frac{L_{\mathrm{sl}} + L_{\mathrm{M}}}{L_{\mathrm{M}}}\right)^2 R_{\mathrm{r}}. \tag{2.22}$$

Now, the induction machine voltage equations can be expressed as

$$\frac{\mathrm{d}\boldsymbol{\psi}_{\mathrm{s}}^{\mathrm{s}}}{\mathrm{d}t} = \boldsymbol{u}_{\mathrm{s}}^{\mathrm{s}} - R_{\mathrm{s}}\boldsymbol{i}_{\mathrm{s}}^{\mathrm{s}}, \tag{2.23}$$

$$\frac{\mathrm{d}\boldsymbol{\psi}_{\mathrm{R}}^{\mathrm{s}}}{\mathrm{d}t} = -R_{\mathrm{R}}\boldsymbol{i}_{\mathrm{R}}^{\mathrm{s}} + j\omega_{\mathrm{m}}\boldsymbol{\psi}_{\mathrm{R}}^{\mathrm{s}}. \tag{2.24}$$

The stator and the rotor flux linkages then become, respectively

$$\boldsymbol{\psi}_{\mathrm{s}}^{\mathrm{s}} = L_{\mathrm{M}}(\boldsymbol{i}_{\mathrm{s}}^{\mathrm{s}} + \boldsymbol{i}_{\mathrm{R}}^{\mathrm{s}}), \tag{2.25}$$

$$\boldsymbol{\psi}_{\mathrm{R}}^{\mathrm{s}} = \boldsymbol{\psi}_{\mathrm{s}}^{\mathrm{s}} + L_{\sigma}\boldsymbol{i}_{\mathrm{R}}^{\mathrm{s}}. \tag{2.26}$$

2.3 Losses of an induction motor

Over the years, numerous studies conducted around the world have shown that electric motors consume a significant amount of the generated electric energy. An article from 1994 shows that even over 25 years ago motors consumed over 50 % of the total produced electric energy [13]. A paper on energy consumption in Germany from 2015 states that the industry consumes over 50 % of the electric energy produced in that country, and 72 % of it is used on operating electric drives [14], which provide the control for electric motors. Moreover, a breakdown of electricity consumption in

the United States informs that 48.2 % of electricity in the commercial sector was consumed in 2014 by electric drives [15]. Therefore, it is evident that motor efficiency is essential.

Efficiency of any electrical motor is defined as

$$\eta = \frac{P_{\text{out}}}{P_{\text{in}}}, \tag{2.27}$$

where P_{in} is the input power, i.e. electrical power fed to the motor, and P_{out} is the output power, i.e. mechanical power at the rotor shaft. The direct method of determining the efficiency is to directly measure the consumed and the provided power at the shaft of the motor [16]. The input and output powers may be measured by performing calorimetric tests, as was done in [17]. Despite being a simple method for efficiency determination, the accuracy of the calorimetric measurements decreases for motors with high efficiency [17]. Based on the principle of energy conversion, the power balance of an electrical motor is defined as [18]

$$P_{\text{in}} = P_{\text{loss}} + \frac{\mathrm{d}W_{\text{f}}}{\mathrm{d}t} + T\omega_{\text{m}}, \tag{2.28}$$

where P_{loss} is the total power loss, W_{f} is the energy of the electromagnetic field and T is the electromagnetic torque. Therefore, in order to determine the efficiency of a simulated electrical machine, it is crucial to compute the power losses accurately. Based on their nature and origin, the total power loss of an electrical motor can be divided into following:

- iron losses in the magnetic circuit,
- resistive losses in the stator and the rotor conductors,
- additional losses,
- mechanical losses.

Following subsections describe the types of losses and how they are modelled for the case of an induction motor. Traditional ways of calculating the losses and the results of recent research are presented. Iron losses are studied especially thoroughly.

2.3.1 Iron losses

Iron (or core) losses in an induction machine are caused by the alternating flux in the magnetic circuit of the machine. Although they occur in both the stator and the rotor, the stator iron loss is higher because the stator frequency is rather higher than the rotor frequency [19]. Iron loss is composed of hysteresis and eddy-current losses, while excess loss is commonly added to increase the accuracy of the model [20]:

$$P_{\text{Fe}} = P_{\text{Hy}} + P_{\text{Ft}} + P_{\text{ex}}. \tag{2.29}$$

This equation is knows as Bertotti's iron loss model. Each component is explained in the upcoming text, followed by the proposed iron loss models.

Hysteresis loss

Inside permanent magnets and ferromagnetic materials there are magnetic domains separated from each other by walls. If an external magnetic field affects the material, the walls move after which the domains start turning in the direction of the external field [9]. The process of reorientating the domains causes a loss of energy. Since this reorientation does not happen immediately after the external field is removed – magnetic flux strength "lags" the field strength forming a hysteresis curve, this energy loss is known as hysteresis loss [19].

According to Equation 3.6, permeability of a material μ is the ratio between the magnetic flux strength $\boldsymbol{B}$ and the magnetic field strength $\boldsymbol{H}$. Even though it is sometimes approximated as constant, $\mu = \mu_0\mu_\mathrm{r}$, where $\mu_0 = 4\pi \cdot 10^{-7}\frac{H}{m}$ is the permeability of vacuum or air and μ_r is the relative permeability of the material, this relation is actually highly nonlinear and multi-valued (as explained above) forming a hysteresis loop, as is shown in Fig. 5.

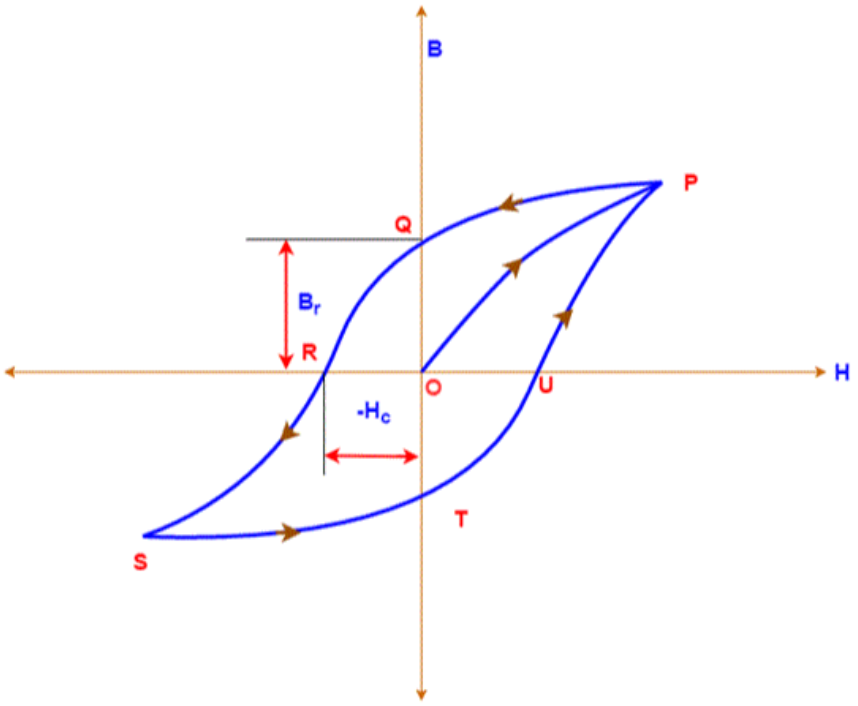

Figure 5: A hysteresis ($\boldsymbol{B} - \boldsymbol{H}$) loop [21]

In Fig. 5, the magnetisation starts from point O, the field strength and the flux strength increase until the saturation point P. When the field strength is decreased, the flux strength decreases as well, but less gradually, and at the point Q, $\boldsymbol{H} = 0$, while there is still a residual flux strength with a positive value, $\boldsymbol{B} = \boldsymbol{B_r}$. The field strength is further decreased and at point R, $\boldsymbol{B}$ reaches 0, while $\boldsymbol{H}$ is at the negative coercive value, $-\boldsymbol{H_c}$. Further decrease of $\boldsymbol{H}$ leads to the negative saturation point S, and so on as the field strength is increased again. This described path is called the

magnetisation curve, and the area inside the curve represents the energy lost during one cycle of magnetisation and demagnetisation, which can be calculated as a line integral [9]:

$$W_{\mathrm{Hy}} = V \oint H dB, \tag{2.30}$$

where V is the volume of the magnetic material. Due to alternating current, the hysteresis loss P_{Hy} depends on the frequency: $P_{\mathrm{Hy}} = fW_{\mathrm{Hy}}$, which leads to a form of Steinmetz's equation [22] adapted by Jordan [23]:

$$P_{\mathrm{Hy}} = C_{\mathrm{Hy}} f B_{\mathrm{max}}^2, \tag{2.31}$$

where C_{Hy} is an empirical constant and the exponent n is typically in the range [1.5 2.5].

It was shown in [24] that hysteresis loss can be separated into two components: alternating and rotational losses. The alternating hysteresis loss is caused by the variation of amplitude of $\boldsymbol{B}$ in time, while the rotational hysteresis loss results from the angle between $\boldsymbol{B}$ and its time derivative [24].

Eddy-current loss

According to Faraday's law, alternating flux in the iron core induces voltage in the core: $\varepsilon = -\frac{d\Phi}{dt}$. The induced voltage then results in circulating eddy-currents in the material. The thicker the conductive material, the higher eddy-currents are induced [9]. Therefore, to reduce the eddy-currents in the material, thin magnetic sheets, or laminations, are used instead. The area of one lamination is much smaller than the area of one single block of iron, which then increases the resistance of the sheets, resulting in decreased eddy-currents (Fig. 6). Laminations are insulated from each other in order to prevent the circulation of eddy-currents across multiple sheets.

The eddy-current loss depends on the thickness of the lamination d, its volume V, frequency f, peak value of the magnetic flux strength B_{max} and resistivity of the material ρ as

$$P_{\mathrm{Ft}} = \frac{V \pi^2 f^2 d^2 B_{\mathrm{max}}^2}{6\rho}, \tag{2.32}$$

which is in accordance with Jordan's extension of Steinmetz's equation:

$$P_{\mathrm{Ft}} = C_{\mathrm{Ft}} f^2 B_{\mathrm{max}}^2, \tag{2.33}$$

where C_{Ft} is an empirical constant.

Excess losses

The "classical" model of iron losses does not include the excess loss. However, in many cases this simplification is insufficiently accurate [20]. In order to improve the accuracy of the calculated losses, excess losses are defined as: $P_{\mathrm{ex}} = P_{\mathrm{Fe}} - P_{\mathrm{Hy}} - P_{\mathrm{Ft}}$. Bertotti introduced so-called magnetic objects (domains, as explained in Hysteresis

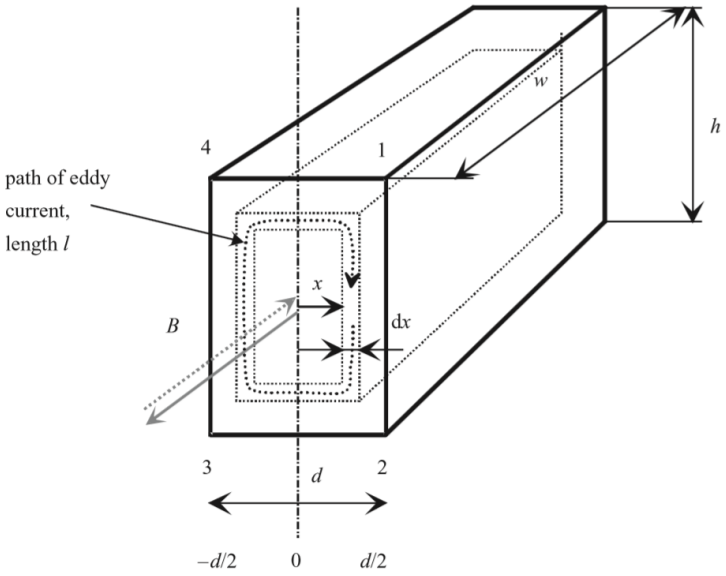

Figure 6: Eddy-currents in a sheet material [9]

section) and defined the factor C_{ex} in terms of the said active magnetic objects and the microscopic eddy-currents caused by the movement of domain walls [25]. Excess losses can then be calculated as

$$P_{\text{ex}} = C_{\text{ex}} f^{1.5} B_{\text{max}}^{1.5}. \tag{2.34}$$

According to [24], excess loss primarily occurs in the case of alternating field.

Analytical approach to iron loss modelling

In the previous sections, the "traditional" way of calculating iron losses was presented. Such equations are often used in FEM calculations and in post-processing, and they often require the knowledge of the physical model of the machine (such as dimensions or material properties). However, for a real-time simulation of an analytical model, this is not convenient. This section analyses different approaches to modelling the iron losses.

Quite commonly, the stator iron loss is accounted for in single phase equivalent circuit models by placing a constant resistor in parallel to the stator inductance or in parallel to the magnetising inductance [1]. Since such resistance depends on the square of frequency, only eddy-current loss can be modelled this way. In [1], Slemon suggested a way to present the stator core loss with a resistor of nonlinear resistance, but without providing an explicit function. In [26], [27] and [28], Levi et al. studied the impact of the iron losses when the machine is supplied with a vector control scheme. They performed no-load tests utilising a PWM inverter at a range of frequencies higher than the rated frequency in order to determine the frequency dependence of the iron loss resistance. They have proved the importance of including the iron losses in an analytical machine model. Based on the mathematical model

presented in [29], Ranta et al. developed a nonlinear iron loss resistance model in [5]. Their work is presented below.

In order to model both the eddy-current and the hysteresis losses of an induction machine, Ranta et al. proposed the following resistance function:

$$R_{\mathrm{Fe}}(u, \psi_{\mathrm{s}}) = \frac{R_{\mathrm{Ft}}}{1 + k\psi_{\mathrm{s}}^{n-1}/u}, \tag{2.35}$$

where R_{Ft} is a positive constant, k is a non-negative constant and the exponent n is typically in the range [1...2]; ψ_{s} is the stator flux magnitude and $u = ||\boldsymbol{u}_{\mathrm{s}} - R_{\mathrm{s}}\boldsymbol{i}_{\mathrm{s}}||$ is the magnitude of the voltage over the iron loss resistor. The resistor is placed in parallel to the stator resistance and the Γ model is utilised (Fig. 7). Constant resistance R_{Ft} is related to the eddy-current losses, while the flux- and voltage-dependent nonlinear resistance

$$R_{\mathrm{Hy}}(u, \psi_{\mathrm{s}}) = \frac{R_{\mathrm{Ft}}}{k}\frac{u}{\psi_{\mathrm{s}}^{n-1}} \tag{2.36}$$

represents the hysteresis loss.

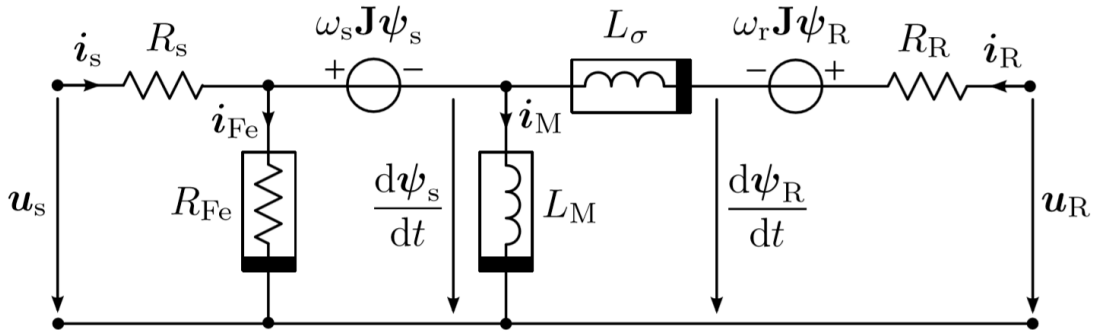

Figure 7: Γ model of an induction machine in synchronous coordinates with an iron loss resistor [5]

Instantaneous iron losses are then calculated as

$$p_{\mathrm{Fe}} = p_{\mathrm{Ft}} + p_{\mathrm{Hy}} = \frac{u^2}{R_{\mathrm{Ft}}} + \frac{k\psi_{\mathrm{s}}^{n-1}u}{R_{\mathrm{Ft}}}, \tag{2.37}$$

where p_{Ft} is the eddy-current loss and p_{Hy} is the hysteresis loss. Steady-state iron loss is then derived as

$$P_{\mathrm{Fe}} = \frac{\omega_{\mathrm{s}}^2\psi_{\mathrm{s}}^2 + k|\omega_{\mathrm{s}}|\psi_{\mathrm{s}}^n}{R_{\mathrm{Ft}}}, \tag{2.38}$$

where ψ_{s} is the constant magnitude of stator flux and ω_{s} is the constant angular frequency of the flux. Parameters for this model are obtained from fitting Equation 2.38 to the iron losses computed in FEM analysis or measured iron losses from laboratory experiments. The least-squares curve fitting algorithm is used for data fitting.

The proposed model [5] is suitable for real-time applications (for example, control) and time-domain simulations. Both losses that originate from the rotation of the flux vector and the pulsation of the flux vector magnitude are included. The model can be used for calculating iron losses in a wide range of frequencies with high accuracy, which is especially improved at low frequencies compared to conventional models (such as constant iron loss resistance). In this case, excess losses are omitted.

2.3.2 Resistive losses

In the case of many machines, resistive losses are the dominant loss component [9]. Resistive (or Joule) losses of an induction machine are composed of the loss in the stator copper winding and the loss in the rotor bar. Generally, resistive losses are calculated as [30]

$$P_{\text{res}} = \int_V \frac{1}{\sigma} \boldsymbol{J}^2 dV, \tag{2.39}$$

where σ is the conductivity, $\boldsymbol{J}$ is current density and V is the volume of the conductor. For the stator winding with m phases, resistive loss can be calculated using the following equation [9]:

$$P_{\text{res,s}} = m R_{\text{s}} I_{\text{s}}^2, \tag{2.40}$$

where I_{s} denotes the current in one parallel path of the stator winding. In some cases, it is enough to approximate R_{s} as the DC resistance of one phase: $R_{\text{s}} = R_{\text{DC}}$. In [31], the DC resistance of one phase is defined as

$$R_{\text{DC}} = \frac{N l_{\text{av}}}{\sigma_{\text{Cu}} S_{\text{Cu}}}, \tag{2.41}$$

where N denotes the number of turns in the winding of the stator, l_{av} is the average length of one turn, σ_{Cu} is the specific conductivity of copper, while S_{Cu} denotes the cross-sectional area of the conductor [31]. The specific conductivity of copper is highly dependent on the temperature, therefore R_{DC} significantly varies with the running machine temperature as well [9].

However, considering only the DC resistance omits the skin effect on resistance. Alternating current in the winding induces an alternating flux, resulting in the eddy-currents on the surface of the conductors, which is known as skin effect [9]. The eddy-current loss represents the difference between total resistive loss and the DC resistive loss [32]. The AC resistance is defined as

$$R_{\text{AC}} = k_{\text{R}} R_{\text{DC}}, \tag{2.42}$$

where k_{R} is the resistance factor defined in [9]. The total (AC) resistive loss of the stator can be presented as the sum of DC resistive and eddy-current losses [33].

Resistive loss of the rotor cage is defined as

$$P_{\text{res,r}} = \int_V -\boldsymbol{J} \cdot \frac{\partial \boldsymbol{A}}{\partial t} dV. \tag{2.43}$$

Equation 2.43 includes the loss in the rotor bars as well as the loss in the end-rings of the rotor cage [30]. Rotor resistive loss can be calculated in a similar way as the stator resistive loss:

$$P_{\mathrm{res,r}} = mR_{\mathrm{R}}I_{\mathrm{R}}^2, \tag{2.44}$$

where R_{R} and I_{R} are the rotor resistance and current, respectively, referred to the stator [31]. Total rotor resistance is defined as

$$R_{\mathrm{r}} = R_{\mathrm{bar}} + \frac{R_{\mathrm{ring}}}{2\sin\frac{\pi p}{Q_{\mathrm{r}}}^2}, \tag{2.45}$$

where R_{bar} is the rotor bar resistance and R_{ring} is the end-ring resistance, while the argument of the sine function is angular phase shift of the bar currents [31]. The referring factor is a coefficient between R_{r} and R_{R} and the equation can be found in [31].

2.3.3 Additional losses

Additional losses account for all the electromagnetic losses that are not included into resistive and iron losses and thus they are sometimes represented as a difference of the total loss and the sum of resistive, iron and mechanical losses [34]. They are difficult to measure or calculate [16] and therefore the convention is to assume additional losses to be 0.5 % of the input power of an induction motor for the case when the motor efficiency is calculated indirectly from the loss measurements, according to IEC standards [9]. (However, in [31] the authors decided to use 1.2 % of input power instead.) If the resistive losses are calculated from the DC resistance of the winding, additional losses include losses in the conductors caused by the skin effect; if iron losses are calculated from the no-load test, then additional losses include the losses caused by the load current and its harmonics in windings, laminations, machine frame, etc. [9]. Additional losses are proportional to the load current to the power of two and to the frequency to the power of 1.5: $P_{\mathrm{ad}} \sim I^2 f^{1.5}$.

Over the years, scientists have been trying to improve the vague definition and ways to estimate the additional losses or more precisely, stray load losses (SLL). In [35], Chalmers et al. divided the SLL of a squirrel-cage induction motor to fundamental and high-frequency components. Fundamental-frequency components comprise eddy-current losses in the stator conductors due to the stator slot-leakage flux, losses due to end-region leakage fluxes and loss at the ends of the stator core due to skew leakage flux [35]. High-frequency components comprise rotor and stator loss due to mmf harmonics resulting from stator load current [35]. Jimoh et al. defined the stray load losses as losses mainly originating from the saturation in magnetic materials, space harmonics, leakage flux and imperfections of the rotor bar insulation. In [36], they gave a detailed overview of various methods of estimating the stray load losses, addressing the SLL in the windings, end leakage-losses, additional losses in the teeth of the machine, skew-leakage losses, SLL due to interbar currents and saturation.

In [37], the authors defined SLL as the difference of output power and input power, no load iron loss, joule losses and mechanical losses. They suggested calculating the SLL by the following equation:

$$P_{\text{stray}} = k\omega_{\text{s}}^{k_1} I_{\text{l}}^{k_2}, \tag{2.46}$$

where ω_s is the fundamental frequency, I_{l} is the line current, and parameters k, k_1, k_2 can be obtained by data fitting to the measurement results.

2.3.4 Mechanical losses

Apart from the electromagnetic losses, electrical machines suffer mechanical losses as well. Most prominent causes of the mechanical losses are bearing friction and windage. Losses due to the bearing friction depend on the shaft speed, load on the bearing as well as the bearing type and properties. Windage loss is caused by the friction between the rotating machine parts and the surrounding air. This loss highly depends on the rotating speed [9]. In [34], mechanical losses were calculated during no-load test by subtracting the iron loss from the total constant losses. In [31], windage losses were neglected and mechanical losses were approximated only by the bearing friction loss. The detailed calculation of the mechanical losses of a squirrel-cage induction motor are given in [38]. However, mechanical losses are not investigated any further in this thesis.

2.4 Magnetic saturation

The previous section described different types of induction motor losses. This section explains the magnetic saturation as well as approaches to modelling this phenomenon.

In order to improve the torque production, induction machines are often built in a way to be a little saturated in the nominal point of operation [19]. Saturation appears mostly in the teeth of stator and rotor (in some cases in the yoke as well) and since these machine parts belong to the main flux path, increased main flux causes the saturation of the magnetising inductance [19]. Furthermore, the main flux may strongly depend on the load (or the rotor current) [39], which in turn affects the inductances. This dependency of the main flux on the rotor current is even more prominent in the case of a machine with skewed or closed rotor slots [40]. Moreover, rotor current considerably affects the rotor leakage inductance as well [40]. Naturally, models with constant-valued parameters, such as the basic T-model described in Section 2.2, cannot account for this nonlinear phenomenon. However, including this variation in inductance would improve the performance of the model.

Over time, various approaches to include the magnetic saturation into the model have been proposed. Inclusion of magnetic nonlinearity in T, Γ and inverse-Γ models was analysed in [1]; however, no equation for the nonlinear inductance was given. This phenomenon was also investigated in [41] and a simple, linear representation of the saturation characteristic was proposed. Transformation of the T-model into the proposed π-model was performed in [42]; this way the magnetic saturation was accounted for. A more advanced model and explicit equations were proposed in

[3]. In this paper, the simple T-model was improved by implementing the following nonlinear functions for magnetising and rotor leakage inductance, respectively:

$$L_{\mathrm{m}}(\psi_{\mathrm{m}}, \psi_{\mathrm{r}\sigma}) = \frac{L_{\mathrm{mu}}}{1 + \alpha\psi_{\mathrm{m}}^{a} + \frac{\gamma L_{\mathrm{mu}}}{d+2}\psi_{\mathrm{m}}^{c}\psi_{\mathrm{r}\sigma}^{d+2}}, \tag{2.47}$$

$$L_{\mathrm{r}\sigma}(\psi_{\mathrm{m}}, \psi_{\mathrm{r}\sigma}) = \frac{L_{\mathrm{r}\sigma\mathrm{u}}}{1 + \beta\psi_{\mathrm{r}\sigma}^{b} + \frac{\gamma L_{\mathrm{r}\sigma\mathrm{u}}}{c+2}\psi_{\mathrm{m}}^{c+2}\psi_{\mathrm{r}\sigma}^{d}}, \tag{2.48}$$

where L_{mu} and $L_{\mathrm{r}\sigma\mathrm{u}}$ are unsaturated magnetising and rotor leakage inductance, respectively, and $\{\alpha, \beta, \gamma, a, b, c, d\} \geq 0$ are constants (values of which are identified by data fitting) [3]. These formulas fulfil the reciprocity condition [3]:

$$\frac{\partial i_{\mathrm{m}}}{\partial \psi_{\mathrm{r}\sigma}} = \frac{\partial i_{\mathrm{r}}}{\partial \psi_{\mathrm{m}}}. \tag{2.49}$$

Apart from modelling the dependency of the magnetising inductance on the main flux and the dependency of the leakage inductance on the leakage flux, Equations 2.47 and 2.48 also account for the mutual saturation. Mutual saturation represents the effect of the main flux on the leakage inductance, as well as the effect of the rotor current on the magnetising inductance. This phenomenon is characteristic for induction machines with closed or skewed rotor slots [3], [40]. However, if the effect of mutual saturation is not prominent in the modelled machine, parameter γ can be set to 0, which leads to simplified equations proposed in [43]. Similar approach to modelling the magnetic saturation was analysed in [19]. In [44] Equation 2.47 (with the simplification $\gamma = 0$) was applied to the transformed magnetising inductance L_{M} of a Γ-model, while the leakage inductance L_{σ} was assumed constant. Same equation was used in [45] for inductances of an induction machine represented with an inverse-Γ model. Moreover, Equations 2.47 and 2.48 were used in [5] for the transformed magnetising and leakage inductance in a Γ-model.

Equations equivalent to 2.47 and 2.48 for the transformed magnetising and leakage inductance of a Γ-model without considering mutual saturation have the following form, respectively:

$$L_{\mathrm{M}}(\psi_{\mathrm{s}}) = \frac{L_{\mathrm{Mu}}}{1 + \alpha\psi_{\mathrm{s}}^{a}}, \tag{2.50}$$

$$L_{\sigma}(\psi_{\sigma}) = \frac{L_{\sigma\mathrm{u}}}{1 + \beta\psi_{\sigma}^{b}}. \tag{2.51}$$

2.5 Chapter summary

This chapter provided an overview of the induction motor theory and reviewed the literature relevant for developing an induction motor model. The basic T and Γ-models were analysed. The latter one was chosen as the basis for designing an improved motor model because it contains fewer parameters and is more suitable for control purposes than the former. Induction motor losses were presented and various approaches for modelling and calculating them were discussed. Resistive and

especially iron losses were thoroughly examined as they constitute the majority of the motor electromagnetic loss, whose accurate calculation was one of the main thesis goals. Magnetic saturation theory and models were reviewed, since this phenomenon needs to be included in the model in order to improve its accuracy. The loss and magnetic saturation models described in this chapter will be implemented in an improved induction motor model, using the methods described in the following chapter. The improved model will be presented in Chapter 4.

3 Methods

The previous chapter introduced the background theory of an induction motor, types of models, as well as power losses of such machine. This chapter briefly describes the methods used for developing an induction motor model. Section 3.1 presents Maxwell's equations and explains the fundamental knowledge of finite element method (FEM), which is utilised for obtaining induction motor data, such as equivalent circuit parameters and loss computations, as well as for validating the model. Finite element analysis (FEA) is done in FC-SMEK [30], and Section 3.2 presents this software. Finally, Section 3.3 introduces the least-squares curve fitting algorithm *lsqnonlin*, which is used for data fitting.

3.1 Finite element method

The finite element method is a numerical method widely used for solving problems of various engineering fields, such as fluid flow, thermal or electromagnetic problems. In electrical engineering, FEM is commonly used in analysis or design of electrical machines and computing relevant data, such as power losses. The problem domain is divided into small elements, and the equations that model these simple elements are put together to form the model of the entire domain. The solution is approximated by minimising the associated error function. The modelling in FEM is based on Maxwell's equations, which are used to solve the magnetic field.

3.1.1 Maxwell's equations

Maxwell's equations describe the laws of an electromagnetic field. These four differential equations were originally proposed in 1873 in [46], which is considered as the foundation of the modern theory of electromagnetism [47]. Thus, they are crucial for electrical machine analysis. Moreover, they form the basis for the FEM theory explained in the next section.

Maxwell's equation may be represented in two forms: differential and integral. In the differential form and for the fully dynamic case, they are derived as follows:

$$\nabla \times \boldsymbol{E} = -\frac{\partial \boldsymbol{B}}{\partial t}, \tag{3.1}$$

$$\nabla \times \boldsymbol{H} = \boldsymbol{J} + \frac{\partial \boldsymbol{D}}{\partial t}, \tag{3.2}$$

$$\nabla \cdot \boldsymbol{D} = \rho, \tag{3.3}$$

$$\nabla \cdot \boldsymbol{B} = 0, \tag{3.4}$$

where $\boldsymbol{E}$ is the electric field density [V/m], $\boldsymbol{H}$ is the magnetic field strength [A/m], $\boldsymbol{D}$ is the electric flux density [C/m^2], $\boldsymbol{B}$ is the magnetic flux strength [T], $\boldsymbol{J}$ is the electric current density [A/m^2] and ρ is the electric charge density [C/m^3] [48].

Equation 3.1 is called Faraday's law and it represents how a changing magnetic field effects the electric field, Equation 3.2 is Maxwell's modification of Ampere's circuital law, Equation 3.3 is called Gauss's law and it represents how electric flux density affects the electric charge density and finally, Equation 3.4 shows the solenoidal nature of magnetic flux strength [47].

However, Maxwell's equations are insufficient for a unique determination of the magnetic field, as they lack the relationship between the field and the material [47]. Constitutive relations are required to describe the medium:

$$\boldsymbol{D} = \varepsilon \boldsymbol{E}, \tag{3.5}$$

$$\boldsymbol{B} = \mu \boldsymbol{H}, \tag{3.6}$$

$$\boldsymbol{J} = \sigma \boldsymbol{E}, \tag{3.7}$$

where ε is permittivity [F/m], μ is permeability [H/m] and σ is conductivity [S/m].

Maxwell's equations can also be written in integral form. For the first two equations, integrals are taken over an open surface S or its contour s, and using Stokes's theorem they become [48]

$$\oint_s \boldsymbol{E} \cdot ds = -\int_S \frac{\partial \boldsymbol{B}}{\partial t} \cdot dS, \tag{3.8}$$

$$\oint_s \boldsymbol{H} \cdot ds = \int_S \left(\boldsymbol{J} + \frac{\partial \boldsymbol{D}}{\partial t} \right) \cdot dS. \tag{3.9}$$

The latter two equations may be transformed to the integral form using Gauss's law on region V and its boundary surface S:

$$\oint_S \boldsymbol{D} \cdot dS = \int_V \rho dV, \tag{3.10}$$

$$\oint_S \boldsymbol{B} \cdot dS = 0. \tag{3.11}$$

3.1.2 Magnetic vector potential

In the case of electromagnetic problems, FEM is based on Maxwell's equations described in the previous section. In quasi-static and static problems, displacement current $\boldsymbol{D}$ is neglected in Equation 3.2:

$$\frac{\partial \boldsymbol{D}}{\partial t} \approx 0. \tag{3.12}$$

This leads to the quasi-static approximation of Ampere's circuital law:

$$\nabla \times \boldsymbol{H} = \boldsymbol{J}. \tag{3.13}$$

But even in such case, two equations, 3.4 and 3.13, describe one unknown. In order to simplify this, $\boldsymbol{B}$ is defined by a vector potential $\boldsymbol{A}$, so that

$$\boldsymbol{B} = \nabla \times \boldsymbol{A} \tag{3.14}$$

holds [48]. For any $\boldsymbol{A}$,

$$\nabla \cdot (\nabla \times \boldsymbol{A}) = 0 \tag{3.15}$$

is true by definition. For 3D problems, gauge condition needs to be satisfied as well [48]:

$$\nabla \cdot \boldsymbol{A} = 0. \tag{3.16}$$

In the case of a 2D problem, this condition is satisfied automatically. Permeability of the material was given by Equation 3.6. However, using reluctivity defined as $\nu = \frac{1}{\mu}$ is more convenient instead. Substituting Equation 3.6 with the constitutive relation

$$\boldsymbol{H} = \nu \boldsymbol{B} \tag{3.17}$$

to the quasi-static approximation of Ampere's circuital law (Equation 3.13), partial differential equation of the vector potential is obtained [48]:

$$\nabla \times (\nu \nabla \times \boldsymbol{A}) = \boldsymbol{J}. \tag{3.18}$$

Since in 2D problems vector potential and current density are equal to $\boldsymbol{A} = A(x, y)\boldsymbol{e_z}$ and $\boldsymbol{J} = J(x, y)\boldsymbol{e_z}$ respectively, Equation 3.18 gets simplified to

$$\nabla \cdot (\nu \nabla \cdot A) = -J. \tag{3.19}$$

In many electrical machine problems it is assumed that the axial length of the machine is infinite, so the magnetic field is solved in 2D, for the x-y plane. Such approach is used in this thesis as well, so 3D problems will not be explained in more detail.

3.1.3 Finite elements

When solving any problem in FEM, the first step is to divide the problem area into, as the name of the method suggests, finite elements. This division is performed in such way that the whole problem region is covered with the finite elements, but without overlapping [48]. The process of dividing the problem area into elements is called meshing, and the result of it is called mesh.

Secondly, nodal points or nodes are selected in the problem region. They represent the points in which the field is computed. Since the finite elements are usually triangles or squares, their corners are selected as the nodes.

Next, shape functions are assigned to each node in the mesh, so that each shape function N_i has value 1 in node i, 0 in all other nodes, and a non-zero value in the

elements that share the node i. Shape functions are continuous functions. First-order shape functions are defined for, in the case of triangular finite elements, the nodes that represent the corners of the triangle. However, they can be polynomials of higher order if the accuracy of the solution needs to be increased.

Then, shape functions of each element are transformed into global shape functions. As illustrated in Fig. 8, shape functions $\hat{N}_i$ of a reference element are mapped into global shape functions N_i.

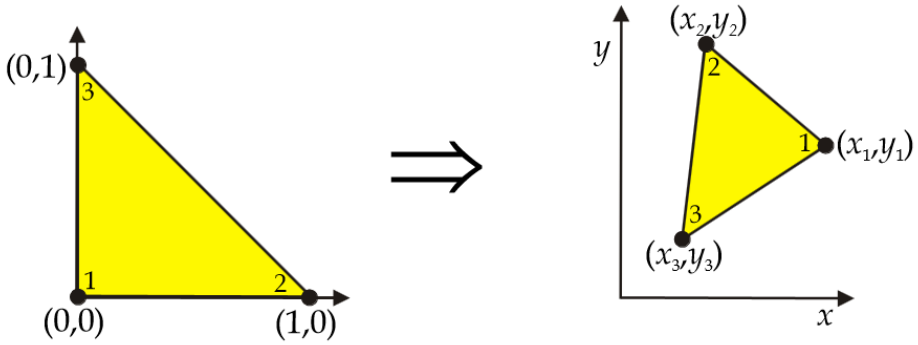

Figure 8: Reference element in reference coordinates is mapped to a global element [49]

Apart from this, in order to estimate the vector potential $\boldsymbol{A}$, boundary conditions need to be defined as well. Common boundary conditions are Dirichlet boundary condition: $\boldsymbol{A} = const.$ (field is parallel to the boundary), homogeneous Neumann condition: $\nu \dfrac{\partial \boldsymbol{A}}{\partial \boldsymbol{n}} = 0$ (field is perpendicular to the boundary) and (anti)periodic boundary: $\boldsymbol{A_1} = \pm \boldsymbol{A_2}$ (used for modelling symmetrical sectors).

Finally, taking the boundary conditions into account, vector potential can be approximated as:

$$\boldsymbol{A} \approx \hat{\boldsymbol{A}}(\boldsymbol{x}) = \sum_{j=1}^{n} a_{\mathrm{j}} N_{\mathrm{j}}(\boldsymbol{x}), \tag{3.20}$$

where n is the total number of nodes in the mesh, N_{j} is the shape function of j-th node, and a_{j} is the value of the vector potential at node j.

3.2 Description of the FEM software

The previous section introduced the finite element method. This section presents FC-SMEK, a program used for FEM simulations.

FC-SMEK is a set of methods designed for 2D finite element analysis (FEA) of induction and synchronous radial flux motors and generators. Due to the periodic symmetry of a machine, FC-SMEK computes the field only for one machine segment and on its sides periodic boundary condition is used [30]:

$$\boldsymbol{A}_1 = \pm \boldsymbol{A}_2, \tag{3.21}$$

Vector potential $\boldsymbol{A}$ is constant-valued on the outer boundary due to the assumption that there is no flux penetrating the outer surface [30]. The number of symmetry segments depends on the number of pole pairs of the machine as well as the number of stator and rotor slots. An example four-pole machine is shown in Fig. 9. This segment contains 12 stator slots and nine rotor slots.

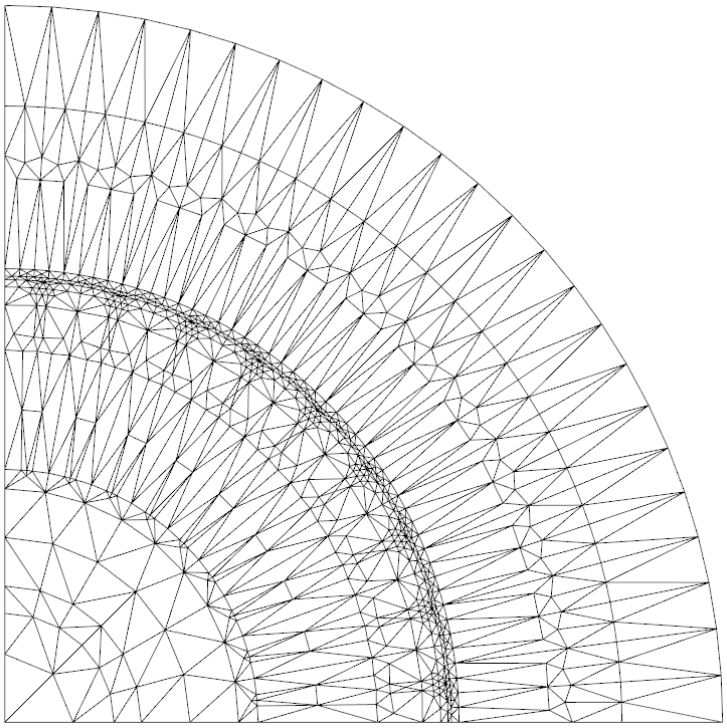

Figure 9: Segment of a cross-section on a four-pole induction machine. The mesh contains 1438 elements and 917 nodes

The FC-SMEK procedure "Mesh" generates a finite element mesh for the geometry of the analysed machine. The required dimensions, slot number and geometry are given as an input to this program. An example of a four-pole induction machine mesh containing 1438 elements and 917 nodes is shown in Fig. 9. The mesh can be created using first, second or third-order triangular elements [30]. It can be seen from Fig. 9 that the mesh inside the air-gap region is more detailed than in other regions. This is necessary in order to acquire accurate field computation.

As FEA in FC-SMEK is in 2D, the vector potential and the current density are equal to $\boldsymbol{A} = A(x,y)\boldsymbol{e_z}$ and $\boldsymbol{J} = J(x,y)\boldsymbol{e_z}$, respectively. In some special problems consisting only of stationary and magnetically linear materials, time-dependence can be omitted. However, for most problems this is not the case and time-dependence needs to be considered. This is achieved by solving the equations by a step-by-step approach. Crank-Nicholson method is used:

$$\boldsymbol{A_{k+1}} = \frac{1}{2}\left\{\frac{\partial \boldsymbol{A}}{\partial t}|_{k+1} + \frac{\partial \boldsymbol{A}}{\partial t}|_{k}\right\}\Delta t + \boldsymbol{A_k}, \tag{3.22}$$

where Δt is a short time interval [30].

Many approximations are made in FC-SMEK, the main one being the assumption of a 2D field. Some 3D effects need to be considered when solving the field problems with a 2D model. First, flux linkages in the stator and rotor resulting from the currents in the end windings are not accounted for in the 2D model. Therefore, these flux linkage values need to be estimated and added in the voltage equations [30]. Next, rotor slots of an induction machine are commonly skewed, and this phenomenon can be taken into account by using a skew factor in the calculations. However, the solution procedure becomes very complex when using this method. Instead, the machine is considered to be formed of multiple thin slices perpendicular to the shaft. The angle between neighbouring slices coincides with the skew factor [30].

The stator and the rotor resistive losses of the analysed machine are calculated according to Equations 2.39 and 2.43, respectively [30]. Iron losses (hysteresis and eddy-current losses) are computed based on Jordan's equations (Equations 2.31 and 2.33).

3.3 Description of the fitting procedure

The previous section presented FC-SMEK, a program used for FEA. This section explains the nonlinear least squares data fitting method *lsqnonlin*.

In order to model acquired data with a certain accuracy, a data fitting technique needs to be used. If the function to which data is fitted is known, nonlinear least squares minimisation problem method can be utilised. A nonlinear least squares problem is defined as an unconstrained minimisation problem and it is in the following form:

$$\underset{x}{\text{minimize}} f(x) = \sum_{i=1}^{m} f_{\text{i}}(x)^2, \tag{3.23}$$

where f_{i} are auxiliary functions and f is the objective function to be minimised [50]. In other words, sum of squares of these auxiliary functions is minimised.

This thesis uses the nonlinear least-squares solver, *lsqnonlin*, provided by MATLAB. This algorithm requires a user-defined function as input and it returns a solution in the form of a vector or an array [51]. This solution vector contains the parameters of the defined function.

The *lsqnonlin* method has two algorithms: "trust region reflective" and "Levenberg-Marquardt". In case when the parameters of the solution vector require certain limits, the former algorithm needs to be used, as the latter cannot handle bound constraints. However, using "Levenberg-Marquardt" algorithm is necessary in case of an underdetermined system of equations, i.e. if the number of equations is lower than the number of elements in the solution vector, because "trust region reflective" cannot solve such problem [51].

3.4 Chapter summary

This chapter presented the methods used in this thesis. Based on Maxwell's equations, Section 3.1 introduced magnetic vector potential and equations necessary for understanding FEM. Program FC-SMEK was briefly described. The time-stepping analysis and the specified procedures will be used for obtaining motor data for the model design, as well as for determining the accuracy of the proposed model. The least squares algorithm *lsqnonlin* will be utilised in parameter identification for the designed induction motor model, as explained in the following chapter.

4 Results and discussion

The previous chapter provided an overview of the methods used for designing and validating the induction motor model. This chapter presents the proposed model and the analysis of the obtained results. Section 4.1 provides the required data of the two motors used for testing, Section 4.2 presents the proposed equivalent circuit, Sections 4.3 and 4.4 explain the modelling of the iron and the resistive losses, respectively, Section 4.5 demonstrates the modelling of the magnetic saturation and Section 4.6 verifies the accuracy of the proposed model by comparing the results to the FEM computations.

4.1 Objective and test motors

The objective of this thesis was to develop an improved analytical induction motor model, as stated in the Introduction (Chapter 1). The improved model was required to be implemented in MATLAB Simulink environment. Electromagnetic loss calculation had to be improved (compared to the traditional analytical model), keeping the model as simple as possible so that it can run in real time. Γ-model presented in Section 2.2 and the model proposed in [5] were used as the basis for the improved model. Some of the equations for calculating the machine losses explained in Section 2.3, as well as the magnetic saturation model (as explained in Section 2.4) were implemented. The FEM-based program FC-SMEK described in Section 3.2 was used to obtain necessary motor data and to validate results. Parameters were identified by data fitting, which was performed using the nonlinear least squares method *lsqnonlin* provided by MATLAB software.

Table 1: Nameplate data of the 45 kW test motor

Parameter	**Value**
Output power [kW]	45
Voltage [V]	400
Current [A]	81.94
Frequency [Hz]	50
Speed [rpm]	1482.65
Torque [Nm]	289.98
Power factor	0.8476
Number of pole pairs	2

In order to design the model as well as to validate the results, two test motors were used in this thesis. Both of them are four-pole squirrel-cage induction motors. The rated powers of these two motors are 45 kW and 250 kW, therefore they will be referred to as "45 kW motor" and "250 kW motor" in the following text. Modelling was based on the 45 kW motor, so the whole modelling process and results will be presented using its data and only the final results will be shown for the 250 kW

Table 2: Nameplate data of the 250 kW test motor

Parameter	Value
Output power [kW]	250
Voltage [V]	500
Current [A]	351.76
Frequency [Hz]	50
Speed [rpm]	1490.66
Torque [Nm]	1603.21
Power factor	0.8493
Number of pole pairs	2

motor. The nameplate data for the 45 kW and the 250 kW motor are given in Tables 1 and 2, respectively.

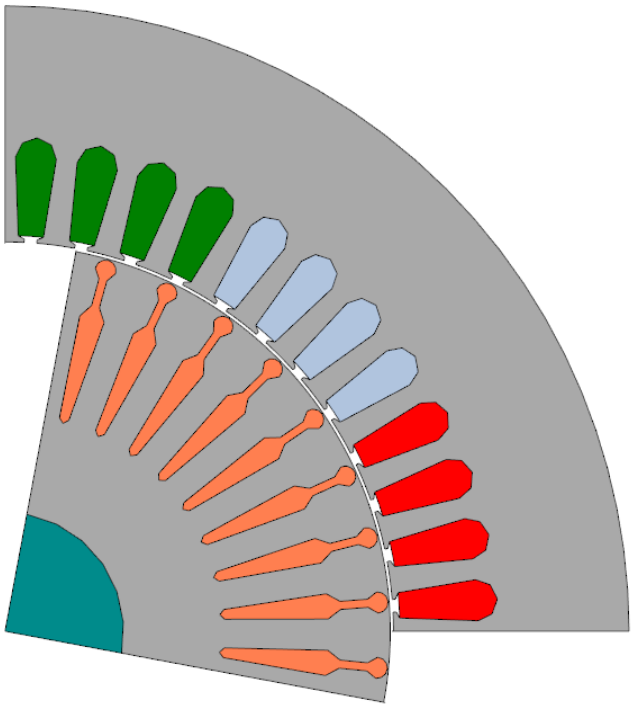

Figure 10: A segment of geometry of the 45 kW motor

Fig. 10 and 11 show the geometries of the 45 kW and the 250 kW motor, respectively. Different colours denote various materials that the motors are made of. Gray colour represents iron in both stator and rotor of the motors. Aluminium bars in the rotor slots of each motor are illustrated in orange. It can be noticed that both motors have closed rotor slots. Stator windings of both machines are made of copper, different colours denote separate phase belts.

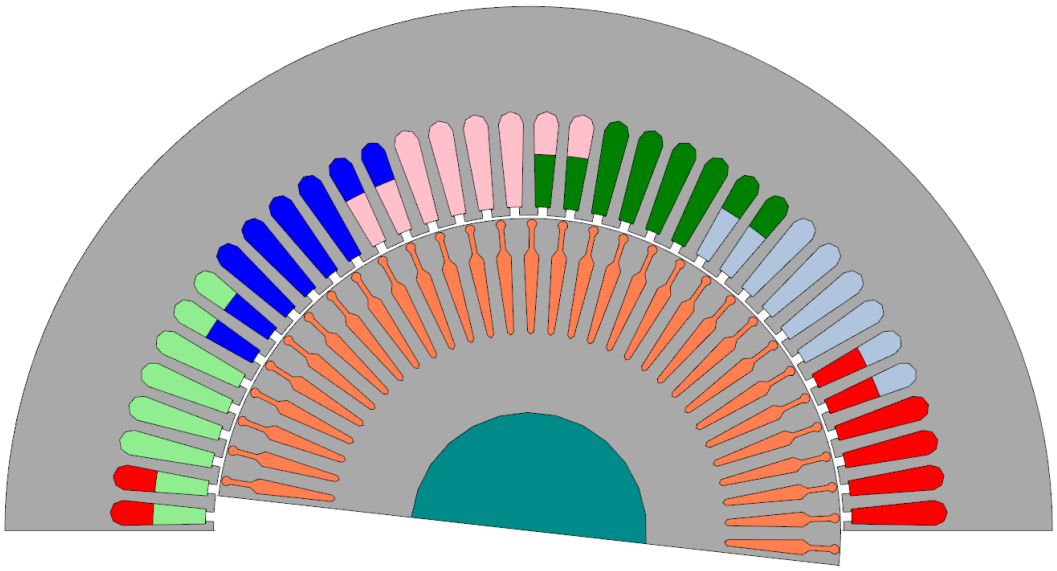

Figure 11: A segment of geometry of the 250 kW motor

Despite having the same number of poles and the same type of rotor, it can be seen that the symmetry segment of the 250 kW motor is much larger than that of the 45 kW motor. This is due to the number of rotor bars in the segment. This results in a mesh with higher number of elements and nodes, which in turn increases the FEM computation time.

4.2 Proposed equivalent circuit

Starting from the basic Γ-model (Fig. 4), an improved induction motor model containing a nonlinear iron loss resistance was proposed in [5], as depicted in Fig. 7. A further improvement which this thesis proposes is separating this iron loss resistance into two components which are the stator and the rotor nonlinear iron loss resistances. The proposed equivalent circuit is shown in Fig. 12.

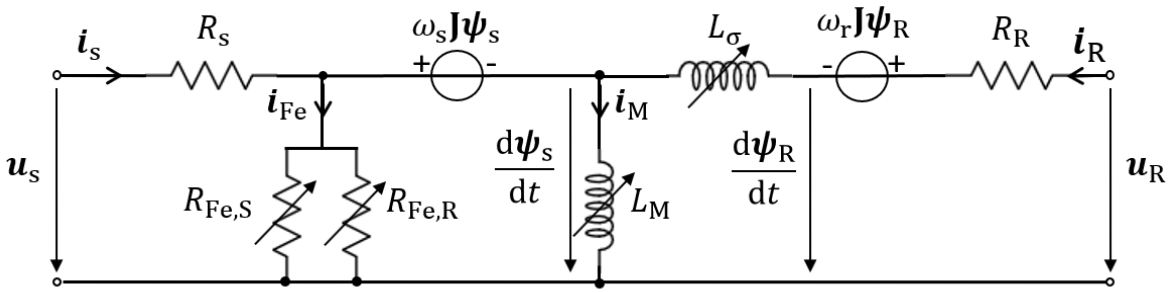

Figure 12: Proposed equivalent circuit

Induction machine voltage equations in synchronous coordinates are defined as

$$\frac{\mathrm{d}\boldsymbol{\psi}_\mathrm{s}}{\mathrm{d}t} = \boldsymbol{u}_\mathrm{s} - R_\mathrm{s}\boldsymbol{i}_\mathrm{s} - j\omega_\mathrm{s}\boldsymbol{\psi}_\mathrm{s}, \tag{4.1}$$

$$\frac{\mathrm{d}\boldsymbol{\psi}_\mathrm{R}}{\mathrm{d}t} = \boldsymbol{u}_\mathrm{R} - R_\mathrm{R}\boldsymbol{i}_\mathrm{R} - j\omega_\mathrm{r}\boldsymbol{\psi}_\mathrm{R}, \tag{4.2}$$

Transforming the voltage equations into stator coordinates leads to Equations 2.23 and 2.24. However, the superscript $^\mathrm{s}$ will from now on be omitted for clarity. As the rotor of the modelled motors is short-circuited, meaning that the rotor voltage is $\boldsymbol{u}_\mathrm{R} = 0$, these equations can be rewritten as

$$\frac{\mathrm{d}\boldsymbol{\psi}_\mathrm{s}}{\mathrm{d}t} = \boldsymbol{u}_\mathrm{s} - R_\mathrm{s}\boldsymbol{i}_\mathrm{s}, \tag{4.3}$$

$$\frac{\mathrm{d}\boldsymbol{\psi}_\mathrm{R}}{\mathrm{d}t} = -R_\mathrm{R}\boldsymbol{i}_\mathrm{R} + j\omega_\mathrm{m}\boldsymbol{\psi}_\mathrm{R}. \tag{4.4}$$

Similarly to Equations 2.25 and 2.26, stator and rotor flux linkages can be derived as, respectively

$$\boldsymbol{\psi}_\mathrm{s} = L_\mathrm{M}(\boldsymbol{i}'_\mathrm{s} + \boldsymbol{i}_\mathrm{R}), \tag{4.5}$$

$$\boldsymbol{\psi}_\mathrm{R} = \boldsymbol{\psi}_\mathrm{s} + L_\sigma\boldsymbol{i}_\mathrm{R}, \tag{4.6}$$

where $\boldsymbol{i}'_\mathrm{s} = \boldsymbol{i}_\mathrm{s} - \boldsymbol{i}_\mathrm{Fe}$. Furthermore, the iron loss current can be calculated as

$$\boldsymbol{i}_\mathrm{Fe} = \frac{\boldsymbol{u}_\mathrm{s} - R_\mathrm{s}\boldsymbol{i}_\mathrm{s}}{R_\mathrm{Fe,e}}, \tag{4.7}$$

where $R_\mathrm{Fe,e}$ is the equivalent iron loss resistance and is defined as stator and rotor iron loss resistances in parallel: $R_\mathrm{Fe,e} = R_\mathrm{Fe,s}||R_\mathrm{Fe,R}$. In addition, the leakage flux is calculated as $\psi_\sigma = L_\sigma\boldsymbol{i}_\mathrm{R}$ and the magnetising current as $\boldsymbol{i}_\mathrm{M} = \boldsymbol{i}'_\mathrm{s} + \boldsymbol{i}_\mathrm{R}$.

It may be observed that the rotor iron loss resistance $R_\mathrm{Fe,R}$ is positioned in the stator side of the equivalent circuit. Results of the FEM computations have shown that the rotor iron loss does not directly depend on the slip, as explained in the following section. Therefore, it is justified to place $R_\mathrm{Fe,R}$ as referred to the stator side.

4.3 Modelling the iron losses

This section first explains the iron loss resistances and the approach to modelling the no load iron losses. Then, parameter identification for the no load iron loss equations is presented. Finally, stray load loss in the stator iron is defined and modelled.

4.3.1 Iron loss resistances

In [5], the iron loss of an induction machine was modelled using one nonlinear resistance R_{Fe}, as explained in Section 2.3.1, Analytical approach to iron loss modelling. This thesis proposes separating the iron loss resistance into stator and rotor iron loss resistances. Based on 2.35, equations for these resistances can be defined as follows: the stator iron loss resistance is formulated as

$$R_{\mathrm{Fe,s}}(u, \psi_{\mathrm{s}}) = \frac{R_{\mathrm{Ft,s}}}{1 + k_{\mathrm{s}} \psi_{\mathrm{s}}^{n_{\mathrm{s}}-1}/u}, \tag{4.8}$$

while the rotor iron loss resistance is given as

$$R_{\mathrm{Fe,R}}(u, \psi_{\mathrm{s}}) = \frac{R_{\mathrm{Ft,R}}}{1 + k_{\mathrm{R}} \psi_{\mathrm{s}}^{n_{\mathrm{R}}-1}/u}, \tag{4.9}$$

where

$$u = \|\boldsymbol{u}_{\mathrm{s}} - R_{\mathrm{s}} \boldsymbol{i}_{\mathrm{s}}\| \tag{4.10}$$

is the voltage over the iron loss resistors, $\psi_{\mathrm{s}} = \boldsymbol{\psi}_{\mathrm{s}}$ is the magnitude of the stator flux, $R_{\mathrm{Ft,s}}$ and $R_{\mathrm{Ft,R}}$ are positive constants, k_{s}, k_{R}, n_{s} and n_{R} are non-negative constants.

Based on Equations 4.8 and 4.9, equivalent iron loss resistance equals to

$$R_{\mathrm{Fe,e}}(u, \psi_{\mathrm{s}}) = R_{\mathrm{Fe,s}}(u, \psi_{\mathrm{s}}) || R_{\mathrm{Fe,R}}(u, \psi_{\mathrm{s}}). \tag{4.11}$$

$R_{\mathrm{Fe,e}}$ accounts for total no load motor iron loss. If the exponents can be approximated as $n_{\mathrm{s}} = n_{\mathrm{R}} = n = 2$, then $R_{\mathrm{Fe,e}}$ can be represented as

$$R_{\mathrm{Fe,e}}(u, \psi_{\mathrm{s}}) = \frac{R_{\mathrm{Ft,e}}}{1 + k_{\mathrm{e}} \psi_{\mathrm{s}}^{n-1}/u}, \tag{4.12}$$

where $R_{\mathrm{Ft,e}}$ models total no load eddy-current loss in the iron of the machine and is equal to

$$R_{\mathrm{Ft,e}} = \frac{R_{\mathrm{Fe,s}} R_{\mathrm{Fe,R}}}{R_{\mathrm{Fe,s}} + R_{\mathrm{Fe,R}}} \tag{4.13}$$

and factor k_{e}, used for calculating the total no load hysteresis machine loss is derived as

$$k_{\mathrm{e}} = \frac{k_{\mathrm{R}} R_{\mathrm{Fe,s}} + k_{\mathrm{s}} R_{\mathrm{Fe,R}}}{R_{\mathrm{Fe,s}} + R_{\mathrm{Fe,R}}}. \tag{4.14}$$

If $n \neq 2$, equations for $R_{\mathrm{Ft,e}}$ and k_{e} become more complicated; however, Equation 4.11 holds for any value of power n.

4.3.2 No load iron loss modelling

Equivalently to [5], each iron loss resistance can be divided into a constant part: $R_{\mathrm{Ft,s}}$ or $R_{\mathrm{Ft,R}}$, which models the eddy-current loss of the stator and the rotor, respectively, and a flux-dependent nonlinear part,

$$R_{\mathrm{Hy,s}}(u,\psi_{\mathrm{s}}) = \frac{R_{\mathrm{Ft,s}}}{k_{\mathrm{s}}}\frac{u}{\psi_{\mathrm{s}}^{n_{\mathrm{s}}-1}} \tag{4.15}$$

which represents the stator no load hysteresis loss and

$$R_{\mathrm{Hy,R}}(u,\psi_{\mathrm{s}}) = \frac{R_{\mathrm{Ft,R}}}{k_{\mathrm{R}}}\frac{u}{\psi_{\mathrm{s}}^{n_{\mathrm{R}}-1}} \tag{4.16}$$

which represents the rotor hysteresis loss. Instantaneous stator and rotor iron losses in the case of no load can then be calculated as, respectively,

$$p_{\mathrm{Fe,s,no\_load}} = p_{\mathrm{Ft,s}} + p_{\mathrm{Hy,s}} = \frac{u^2}{R_{\mathrm{Ft,s}}} + \frac{k_{\mathrm{s}}\psi_{\mathrm{s}}^{n_{\mathrm{s}}-1}u}{R_{\mathrm{Ft,s}}}, \tag{4.17}$$

$$p_{\mathrm{Fe,R}} = p_{\mathrm{Ft,R}} + p_{\mathrm{Hy,R}} = \frac{u^2}{R_{\mathrm{Ft,R}}} + \frac{k_{\mathrm{R}}\psi_{\mathrm{s}}^{n_{\mathrm{R}}-1}u}{R_{\mathrm{Ft,R}}}, \tag{4.18}$$

where $p_{\mathrm{Ft,s}}$ and $p_{\mathrm{Hy,s}}$ are the eddy-current and hysteresis loss in the stator iron and, equivalently, $p_{\mathrm{Ft,R}}$ and $p_{\mathrm{Hy,R}}$ are the eddy-current and hysteresis loss in the rotor iron. These equations are in accordance with Equation 2.37. The total no load iron loss of the machine is naturally equal to the sum of the stator and rotor no load iron loss: $p_{\mathrm{Fe,no\_load}} = p_{\mathrm{Fe,s,no\_load}} + p_{\mathrm{Fe,R}}$. In steady-state, Equations 4.17 and 4.18 can be expressed as

$$P_{\mathrm{Fe,s,no\_load}} = \frac{\omega_{\mathrm{s}}^2\psi_{\mathrm{s}}^2 + k_{\mathrm{s}}\omega_{\mathrm{s}}\psi_{\mathrm{s}}^{n_{\mathrm{s}}}}{R_{\mathrm{Ft,s}}} \tag{4.19}$$

and

$$P_{\mathrm{Fe,R}} = \frac{\omega_{\mathrm{s}}^2\psi_{\mathrm{s}}^2 + k_{\mathrm{R}}\omega_{\mathrm{s}}\psi_{\mathrm{s}}^{n_{\mathrm{R}}}}{R_{\mathrm{Ft,R}}}. \tag{4.20}$$

In order to model the no load stator iron loss using the proposed equation, identifying parameters $R_{\mathrm{Ft,s}}$, k_{s} and n_{s} was required. Therefore, a 2D time-stepping FEA was performed at no load at several operational points. The iron loss was computed at six different frequencies. Three various voltage levels were applied at each frequency. The model expressed by Equation 4.19 was fitted to the FEA results using the *lsqnonlin* method described in Section 3.3. The following parameter values were obtained: $R_{\mathrm{Ft,s}} = 724.92\Omega$, $k_{\mathrm{s}} = 447.42$ and $n_{\mathrm{s}} = 2.11$.

Fig. 13 shows data obtained by FEM (marked with points) as well as the results of fitting (marked with lines). Fig. 13a presents no load stator iron losses at frequencies up to 50 Hz, corresponding to the constant flux region, and three flux levels: 0.37 p.u., 0.74 p.u. and 0.81 p.u. In the case of the 45 kW test motor, these flux levels are equivalent to 0.47 Wb, 0.94 Wb and 1.03 Wb. Fig. 13b shows no load stator

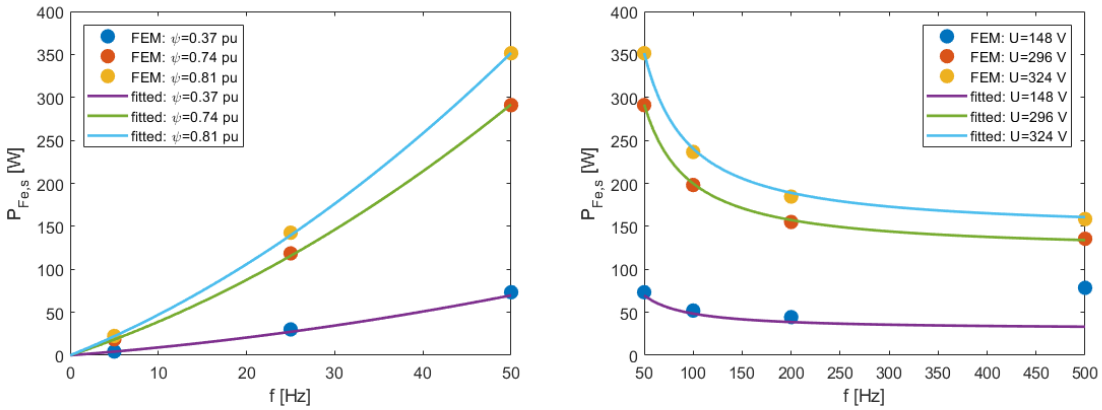

(a) Constant flux region (b) Field weakening region

Figure 13: Parameter identification for the stator no load iron loss

iron losses at frequencies higher than 50 Hz, which correspond to the field weakening region. This means that each line in this graph represents a constant voltage level (148 V, 296 V or 324 V), while the flux decreases, due to it being inversely proportional to frequency.

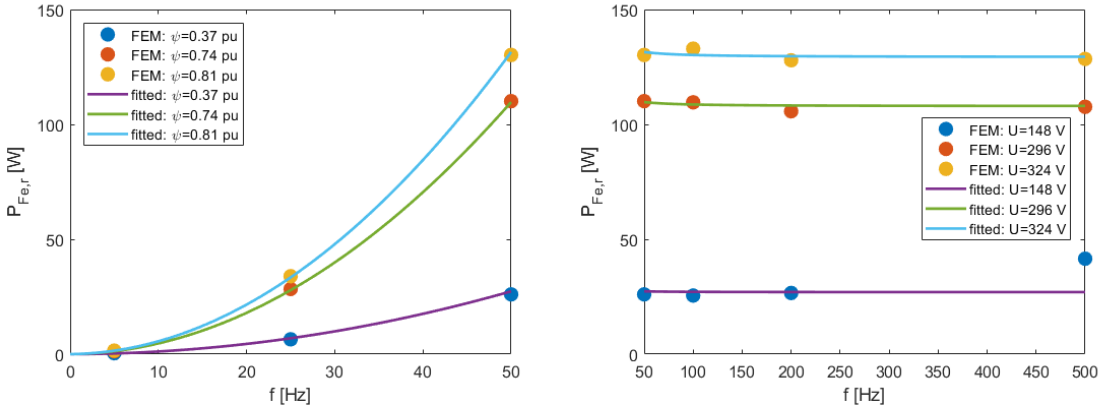

(a) Constant flux region (b) Field weakening region

Figure 14: Parameter identification for the rotor iron loss

Rotor iron loss was computed using FEM at the same operational points. Parameters of Equation 4.20 were obtained using the *lsqnonlin* method as follows: $R_{\mathrm{Ft,R}} = 811.68\Omega$, $k_{\mathrm{R}} = 5.22$ and $n_{\mathrm{R}} = 2.3$. Fig. 14 shows the rotor iron loss computed by FEM and the fitted loss equations. Data in Fig. 14a corresponds to the constant flux region, while the data in Fig. 14b shows the field weakening region, similarly to the previous figure.

It can be seen from Fig. 13 and 14 that the proposed model fits very well to the FEM results. This is in accordance with the results obtained in [5]. As both exponents n_{s} and n_{R} are close to two, the approximation $n_{\mathrm{s}} = n_{\mathrm{R}} = 2$ can be made. Therefore, equivalent resistance which accounts for the total no load iron loss of

the motor $R_{\mathrm{Fe,e}}$ can be written in the form of Equation 4.12, where constants $R_{\mathrm{Ft,e}}$ and k_{e} can be simply derived from Equations 4.13 and 4.14 using the parameters obtained from data fitting. However, calculation of $R_{\mathrm{Fe,e}}$ is kept in its general form (Equation 4.11) because such approximation cannot be applied to every simulated motor.

4.3.3 Stray load loss in the stator iron

In some studies, iron losses are considered constant [34], [52]. However, FEA has shown that the stator iron loss depends significantly on the motor load: the loss increases noticeably with increase in load. Fig. 15 shows the stator iron loss of the 45 kW motor with the increase in load from zero to rated, rising with the steps of 25 % of the rated load. These losses were computed at the rated stator voltage and frequency, varying only the motor load. When comparing the stator iron loss in the no load case with the same loss in the rated load case, an increase of almost 40 % can be seen. This increase in the stator iron loss is in accordance with studies which analysed machine iron loss in detail (such as [53]).

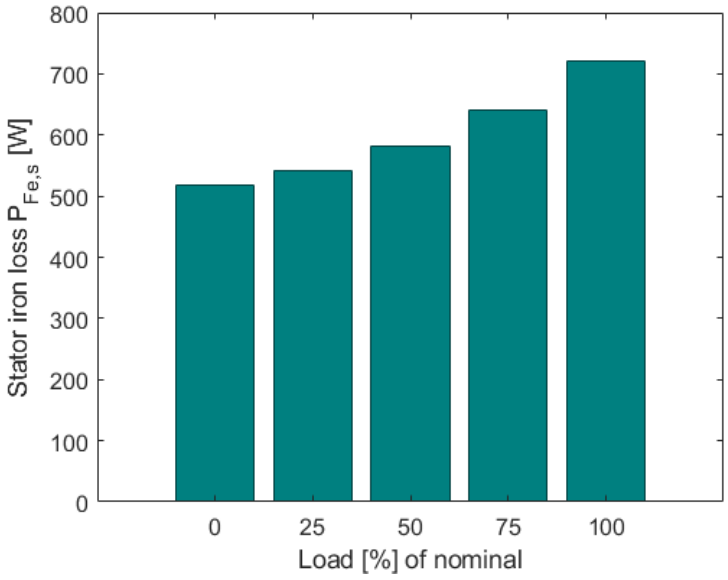

Figure 15: Stator iron loss of the 45 kW motor as a function of load

In order to further analyse the dependency of the iron losses on the change in load, losses in different parts of the stator and the rotor are presented in Fig. 16. Slip variation in this figure corresponds to the change in load from no load to the rated load, the rated slip being equal to 1.157 %. Fig. 16a shows that the loss in the stator yoke is nearly constant; however, losses in the stator teeth and tooth tips contribute to the significant increase of the total loss in the stator iron with increase in load. This result is similar to that reported in [53]. On the other hand, Fig. 16b shows that the loss in rotor teeth is increasing almost linearly with the slip, but the variation of the loss in rotor tooth tips is making the total rotor iron loss almost

constant. The loss in the rotor yoke is well bellow 1 W for any value of the slip within the presented range and therefore it is not visible in the Fig. 16b. This variation in the rotor iron loss slightly differs from the result presented in [53].

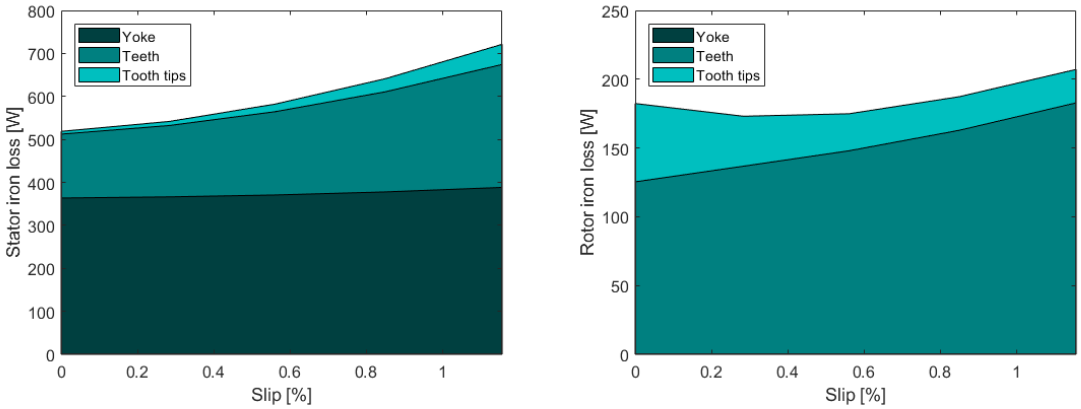

(a) Stator (b) Rotor

Figure 16: Iron losses in different parts of the stator and the rotor of the 45 kW motor

As the total loss in the rotor iron does not increase significantly with the increase in load, Equation 4.18 was found to be modelling this loss with satisfactory accuracy. However, even though Equation 4.17 models stator no load iron loss precisely, it does not account for the loss in the stator iron due to loading. This loss was named the stray load loss (SLL) in the stator iron $p_{\mathrm{Fe,s,SLL}}$ and had to be considered separately:

$$p_{\mathrm{Fe,s,SLL}} = p_{\mathrm{Fe,s}} - p_{\mathrm{Fe,s,\ no\_load}}, \tag{4.21}$$

where $p_{\mathrm{Fe,s}}$ is the total stator iron loss and $p_{\mathrm{Fe,s,\ no\_load}}$ is the stator iron loss in the no load case as calculated using Equation 4.17.

The proposed equation for modelling the stray load loss in the stator iron is as follows:

$$p_{\mathrm{Fe,s,SLL}} = k_1 \omega_{\mathrm{r}}^{n_{\mathrm{s1}}} u_{\mathrm{s}}^{n_{\mathrm{s2}}}, \tag{4.22}$$

where $\omega_{\mathrm{r}} = \omega_{\mathrm{s}} - \omega_{\mathrm{m}} = s\omega_{\mathrm{s}}$ is the angular slip frequency, u_{s} is the stator voltage and k_1, n_{s1} and n_{s2} are non-negative constants. These three parameters need to be identified using *lsqnonlin* method, similarly to no load stator and rotor iron loss. This equation is similar to the equation for the stray load loss proposed in [37].

In order to perform the data fitting, FEA was used to compute the total stator iron loss in various operational points. Three different frequencies, three flux levels and five loading conditions were used as input for the FEM computations, as shown in Fig. 17. The various loading conditions (ranging from no load to rated load) correspond to different slips in each of the graphs (Fig. 17a, 17b and 17c) due to different input frequencies and fluxes in each case. In all the graphs in Fig. 17 points represent the data obtained from FEA, while the lines show the results of fitting this

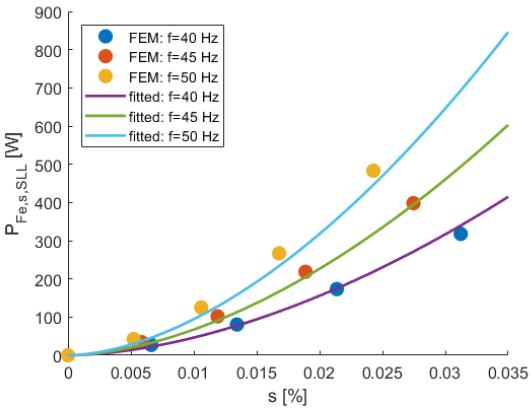

(a) $\psi_s = 0.74$p.u.

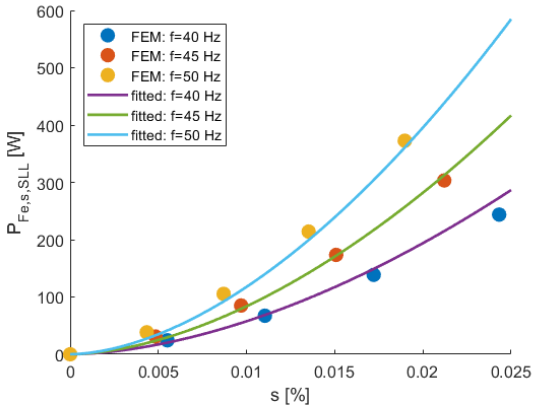

(b) $\psi_s = 0.81$p.u.

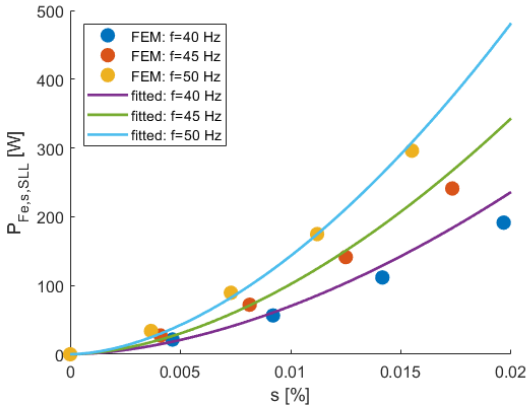

(c) $\psi_s = 0.88$p.u.

Figure 17: Parameter identification for the stray load loss in the stator iron of the 45 kW motor

data to the loss model expressed by Equation 4.22. Following values were identified for the parameters in this equation: $k_1 = 0.0004$, $n_{s1} = 1.75$ and $n_{s2} = 1.86$.

It is important to note that the frequency range which was used for identifying the parameters for the stray load loss in the stator iron is narrower than the range of frequencies used in parameter identification for the no load stator iron loss. This means that the proposed equation could not predict the SLL as accurately as the no load loss in a wide frequency range. Nonetheless, using the sum of the no load loss and the SLL significantly improves the accuracy of the total stator iron loss prediction compared to the case when the stator iron loss is parametrised using only no load data.

4.4 Modelling the resistive losses

The previous section described the modelling of the stator no load iron loss, rotor iron loss, as well as the stray load loss in the stator iron. This section explains the modelling of the stator and rotor resistive losses.

The stator resistive loss is modelled according to Equation 2.40 as

$$p_{\mathrm{res,s}} = 3R_{\mathrm{s}}i_{\mathrm{s}}^2, \tag{4.23}$$

where R_{s} is the stator resistance and i_{s} is the stator current. However, as the rotor resistance is assumed constant, the rotor resistive loss was not modelled accurately using the equivalent equation. In order to account for the loss due to the skin effect in the rotor bars, the following equation was proposed:

$$p_{\mathrm{res,R}} = 3R_{\mathrm{R}}i_{\mathrm{R}}^2 + k_2\omega_{\mathrm{s}}^{n_{\mathrm{R1}}}i_{\mathrm{s}}^{n_{\mathrm{R2}}}, \tag{4.24}$$

where R_{R} is the transformed resistance of the rotor bars, i_{R} is the rotor current, ω_{s} is the stator angular frequency and k_2, n_{R1} and n_{R2} are non-negative constant parameters.

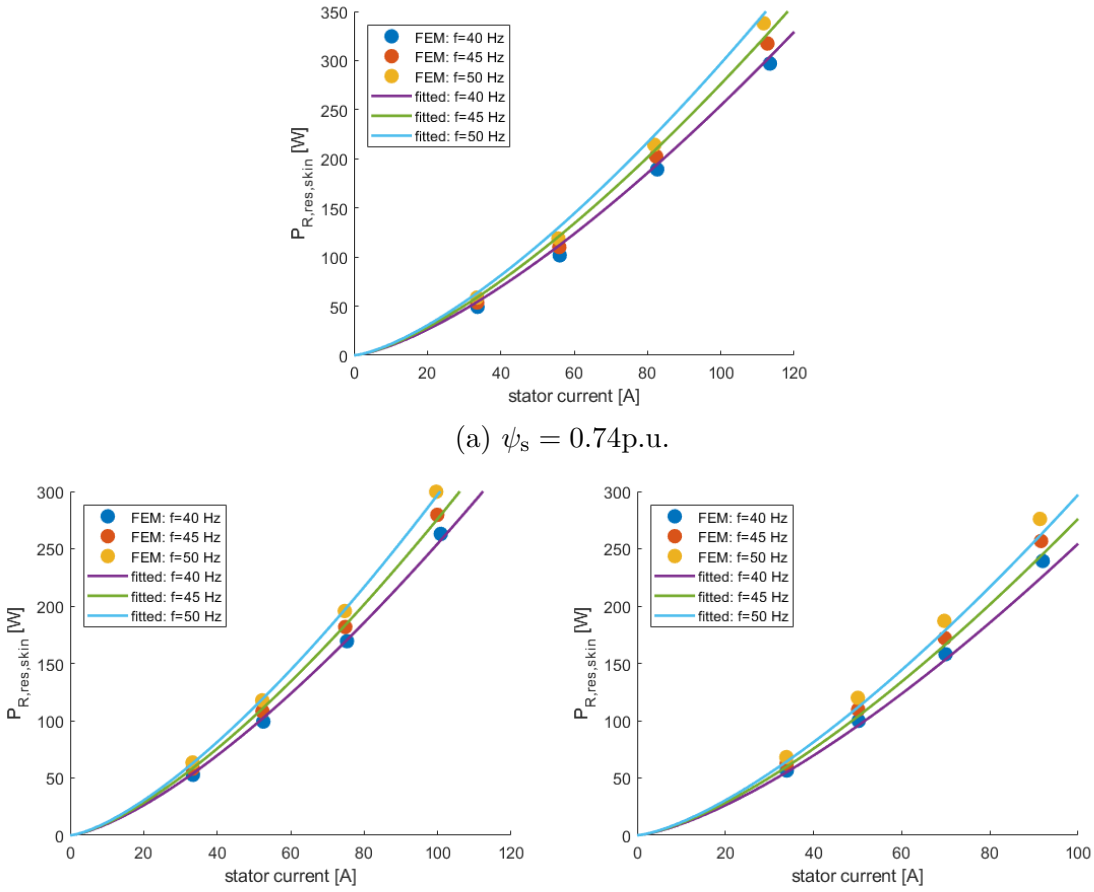

(a) $\psi_{\mathrm{s}} = 0.74$p.u.

(b) $\psi_{\mathrm{s}} = 0.81$p.u.

(c) $\psi_{\mathrm{s}} = 0.88$p.u.

Figure 18: Parameter identification for the loss due to the skin effect in the rotor bars of the 45 kW motor

In order to identify these parameters, FEA was performed at different operational points. Rotor resistive loss was computed at three different frequencies (40 Hz, 45 Hz and 50 Hz), three flux levels (0.74 p.u., 0.81 p.u. and 0.88 p.u., which are

equivalent to 0.94 Wb, 1.03 Wb and 1.12 Wb and are shown in Fig. 18a, 18b and 18c, respectively) and four loading conditions (25 % – 100 % of rated load). The loss due to eddy-currents in the rotor bars $p_{\mathrm{res,R,ft}} = k_2 \omega_{\mathrm{s}}^{n_{\mathrm{R1}}} i_{\mathrm{s}}^{n_{\mathrm{R2}}}$ was calculated as the difference between the total rotor resistive loss obtained from FEA and the $3R_{\mathrm{R}} i_{\mathrm{R}}^2$ loss. MATLAB function *lsqnonlin* was used to fit the data to the proposed equation for $p_{\mathrm{res,R,ft}}$ and the computed parameters are as follows: $k_2 = 0.0081$, $n_{\mathrm{R1}} = 0.7$ and $n_{\mathrm{R2}} = 1.41$.

Fig. 18 shows the values of the eddy-current loss in the rotor bars computed by FEM as points, while the fitted equations for $p_{\mathrm{res,R,ft}}$ are represented with lines in the graphs. Similarly to the stray load loss in the stator iron, parameters for the eddy-current loss in the rotor bars model are identified from the losses computed at a rather narrow frequency range.

4.5 Modelling magnetic saturation

The previous section described how the motor resistive losses were modelled. This section explains modelling the magnetic saturation.

Since induction machines are commonly constructed to be a little saturated in the rated point of operation [19], constant inductance parameters of the Γ-model need to be replaced with nonlinear inductances in order to model this phenomenon. Mutual saturation can be modelled using Equations 2.47 and 2.48. However, according to [3], some of the parameters of the proposed equations complicate the fitting process, so the simplified saturation model was implemented instead. In this thesis the phenomenon of magnetic saturation was modelled using Equation 2.50 for the magnetising inductance: $L_{\mathrm{M}}(\psi_{\mathrm{s}}) = \dfrac{L_{\mathrm{Mu}}}{1 + \alpha \psi_{\mathrm{s}}^a}$ and Equation 2.51 for the leakage inductance: $L_{\sigma}(\psi_{\sigma}) = \dfrac{L_{\sigma \mathrm{u}}}{1 + \beta \psi_{\sigma}^b}$. The parameters of these functions are identified through the data fitting process.

The unsaturated magnetising and leakage inductances L_{Mu} and $L_{\sigma \mathrm{u}}$ in the Equations 2.50 and 2.51 were determined as the constant equivalent circuit parameters. Constants α, a, β and b were identified similarly to the indirect method described in [3]. First, the no load operation of the motor is simulated using FEM at different voltage levels. Due to no load, magnetising current is equal to stator current: $\boldsymbol{i}_{\mathrm{M}} = \boldsymbol{i}_{\mathrm{s}}$, and the main flux is determined as the stator flux in the Equation 2.23: $\boldsymbol{\psi}_{\mathrm{M}} = \dfrac{\boldsymbol{u}_{\mathrm{s}} - R_{\mathrm{s}} \boldsymbol{i}_{\mathrm{M}}}{\omega_{\mathrm{s}}}$. As the rotor current is zero, the magnetising inductance function is equal to the ratio of the main flux and the stator current, $L_{\mathrm{M}} = \dfrac{\psi_{\mathrm{m}}}{i_{\mathrm{M}}}$. Parameters α and a were identified by minimising this cost function.

Then, the operation of the motor was simulated using FEM at various load levels and at different voltages. From the computed values of slip, stator current and stator flux and using the previously obtained values of magnetising current, rotor current can be calculated as $\boldsymbol{i}_{\mathrm{R}} = \boldsymbol{i}_{\mathrm{s}} - \boldsymbol{i}_{\mathrm{M}}$. Leakage flux can then be obtained as $\boldsymbol{\psi}_{\sigma} = \boldsymbol{\psi}_{\mathrm{R}} - \boldsymbol{\psi}_{\mathrm{s}} = \dfrac{R_{\mathrm{R}}}{\omega_{\mathrm{r}}} \boldsymbol{i}_{\mathrm{R}} - \boldsymbol{\psi}_{\mathrm{s}}$. Parameters β and b were identified by equalling the

leakage inductance function to the ratio of the leakage flux and the rotor current and minimising this cost function: $L_\sigma = \dfrac{\psi_\sigma}{i_\mathrm{R}}$.

As for identification of the parameters of the proposed loss functions, the parameters of the inductance functions were identified using the time-stepping FEA and the *lsqnonlin* method. For the 45 kW motor, the parameters were identified as the following: $\alpha = 0.059$, $a = 13.27$, $\beta = 0.0003$ and $b = 20.96$. It can be seen from these parameter values that the saturation of the magnetising inductance is much more prominent than the saturation of the leakage inductance.

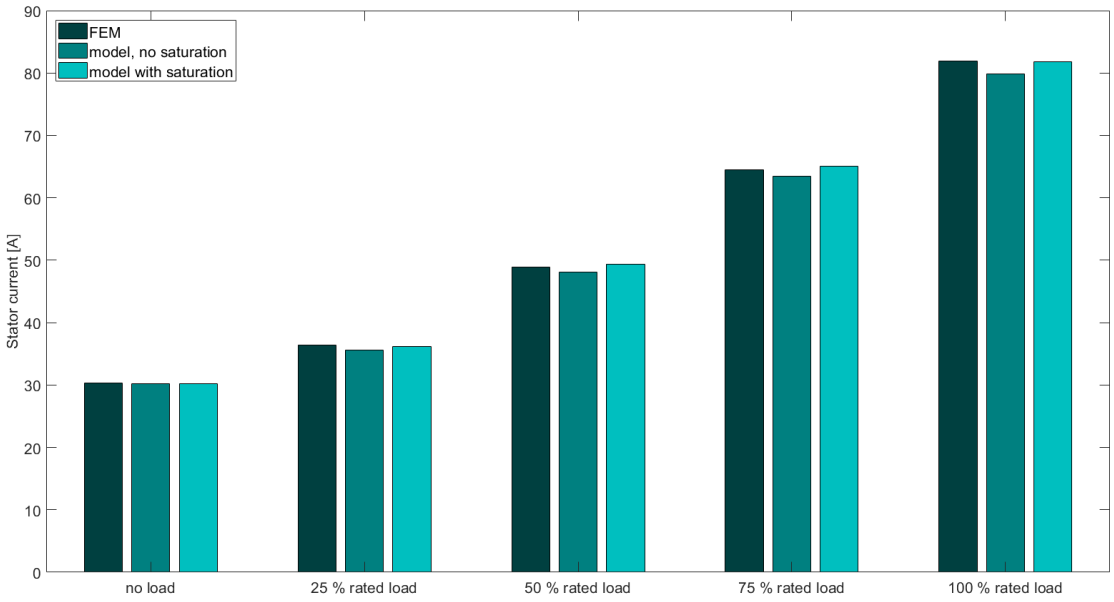

Figure 19: Stator current of the 45 kW motor at different loading conditions

In order to analyse the effect of including the proposed magnetic saturation model, the comparison of the different models was made by calculating the rms value of the stator current at various loading conditions. This comparison of the FEM model, analytical model without magnetic saturation and the improved analytical model which includes the magnetic saturation is shown in Fig. 19. As expected, in the no load case saturation has no effect on the current. As the load increases, magnetic saturation increasingly affects the stator current. In the rated condition, the stator current calculated in FC-SMEK is equal to 81.94 A. The motor model which includes the saturation gives the result very close to the FEM model: 81.81 A. For the same loading condition, the model with no saturation calculation simulates the stator current of only 79.9 A. This result translates to the error of 0.16 % when the magnetic saturation model is used, while the model without magnetic saturation increases the error to 2.49 % as compared to the value computed by FEM. The improvement of including the magnetic saturation model is especially important when the motor is expected to operate at loading conditions close to the rated.

4.6 Proposed model

The previous sections presented the proposed equivalent circuit and described the proposed iron and resistive loss models, as well as the phenomenon of magnetic saturation model. This section compares the improved model to the original one, as well as to the FEM computations.

In summary, this thesis proposes the following loss model:

- stator iron loss comprising eddy-current and hysteresis no load losses as well as the stray load loss and is modelled as $p_{\mathrm{Fe,s}} = \dfrac{u^2}{R_{\mathrm{Ft,s}}} + \dfrac{k_{\mathrm{s}}\psi_{\mathrm{s}}^{n_{\mathrm{s}}-1}u}{R_{\mathrm{Ft,s}}} + k_1\omega_{\mathrm{r}}^{n_{\mathrm{s1}}}u_{\mathrm{s}}^{n_{\mathrm{s2}}}$,
- rotor iron loss composed of eddy-current and hysteresis loss is modelled as $p_{\mathrm{Fe,R}} = \dfrac{u^2}{R_{\mathrm{Ft,R}}} + \dfrac{k_{\mathrm{R}}\psi_{\mathrm{s}}^{n_{\mathrm{R}}-1}u}{R_{\mathrm{Ft,R}}}$,
- stator resistive loss is modelled as $p_{\mathrm{res,s}} = 3R_{\mathrm{s}}i_{\mathrm{s}}^2$,
- rotor resistive loss comprised of the loss in the rotor bars and the skin effect in the bars is modelled as $p_{\mathrm{res,R}} = 3R_{\mathrm{R}}i_{\mathrm{R}}^2 + k_2\omega_{\mathrm{s}}^{n_{\mathrm{R1}}}i_{\mathrm{s}}^{n_{\mathrm{R2}}}$.

The proposed equivalent circuit is shown in Fig. 12. The nonlinear elements in this circuit are the following:

- stator iron loss resistance $R_{\mathrm{Fe,s}}(u,\psi_{\mathrm{s}}) = \dfrac{R_{\mathrm{Ft,s}}}{1 + k_{\mathrm{s}}\psi_{\mathrm{s}}^{n_{\mathrm{s}}-1}/u}$,
- rotor iron loss resistance $R_{\mathrm{Fe,R}}(u,\psi_{\mathrm{s}}) = \dfrac{R_{\mathrm{Ft,R}}}{1 + k_{\mathrm{R}}\psi_{\mathrm{s}}^{n_{\mathrm{R}}-1}/u}$,
- magnetising inductance $L_{\mathrm{M}}(\psi_{\mathrm{s}}) = \dfrac{L_{\mathrm{Mu}}}{1 + \alpha\psi_{\mathrm{s}}^{a}}$ and
- leakage inductance $L_{\sigma}(\psi_{\sigma}) = \dfrac{L_{\sigma\mathrm{u}}}{1 + \beta\psi_{\sigma}^{b}}$.

It is important to note that the iron loss model proposed in [5] (Equation 2.37) was improved in this thesis by separating the stator no load iron loss from the rotor iron loss. In addition, equations for the stray load loss in the stator iron and the eddy-current loss in the rotor bars were proposed in this thesis.

Fig. 20 shows the comparison of the "original" and the improved (proposed) analytical model of the 45 kW motor to the FEM loss computations. The "original" loss model comprises Equation 2.37: $p_{\mathrm{Fe}} = \dfrac{u^2 + k\psi_{\mathrm{s}}^{n-1}u}{R_{\mathrm{Ft}}}$, Equation 2.40: $p_{\mathrm{res,s}} = 3R_{\mathrm{s}}i_{\mathrm{s}}^2$ and Equation 2.44: $p_{\mathrm{res,R}} = 3R_{\mathrm{R}}i_{\mathrm{R}}^2$. However, a slight modification was made to the original model to make the comparison fair: stator and rotor iron losses were separated according to Equations 4.17 and 4.18. The improved model is defined as explained above. FEM results were obtained from the time-stepping analysis with sinusoidal input. The original and the improved analytical model were implemented

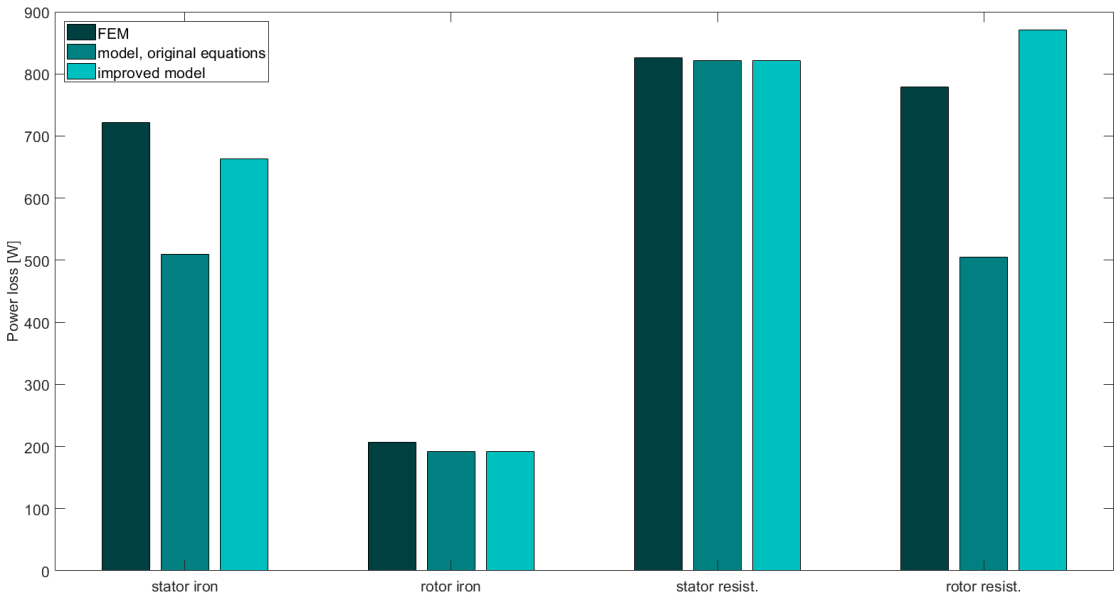

Figure 20: 45 kW motor loss components at the rated load

in MATLAB Simulink and ran with a simple rotor flux oriented vector control with sinusoidal input, which was used in order to make the results comparable. It can be seen from Fig. 20 that the improved stator iron loss model gives a little lower result than FEM, however, this value is closer to FEM than the one obtained from the original model. Similarly, the improved rotor resistive loss model gives a little higher result than FEM, however, this value is closer to FEM than the one obtained from the original model. For the rotor iron loss and the stator resistive loss, both original and improved model give equal results because the same equations were used in both models.

Fig. 21 shows the total electromagnetic (EM) loss of the 45 kW motor at different loading conditions. Total EM loss encompasses the losses in the stator and rotor iron, as well as the resistive losses in the stator and the rotor. All three models, FEM, original and improved analytical model, are the same as described in the previous paragraph. Simulation conditions were the same as described above. It can be seen that the improved model gives much closer result to the FEM model compared to the original analytical model in all loading conditions.

The comparison of the errors in the calculated EM loss for the different loading conditions is shown in Table 3. The error is calculated as error $= \frac{P_{\text{loss,FEM}} - P_{\text{loss,analytical model}}}{P_{\text{loss,FEM}}} \cdot 100[\%]$, where $P_{\text{loss,FEM}}$ is the total EM loss computed by FEM and $P_{\text{loss,analytical model}}$ is the total EM loss calculated from an analytical model, original and improved, as respectively shown in Table 3. It is evident that the error of the original loss model increases with the increase in load. This result is expected because the loss in the stator iron due to loading is not accounted for in this model. Furthermore, the rotor resistive loss in the original model does not include the skin effect in the rotor bars, which further aggravates the total loss prediction of this model. On the other hand,

Table 3: Error in the calculated EM loss of the 45 kW motor

Load [% of rated]	**Error [%]; original model**	**Error [%]; improved model**
0	10.68	0.09
25	15.81	3.00
50	17.14	0.31
75	18.20	1.28
100	19.95	0.57

the error of the improved loss model does not follow such pattern; it does not increase nor decrease with increase in load. This may be explained by the fact that the modelled loss components are fluctuating around the corresponding losses calculated by FEM. For example, the stator iron loss from the improved model is lower than that computed by FEM at any loading condition when the stator frequency is set to 50 Hz, while the rotor resistive loss of the improved analytical model is higher than that computed by FEM at the described operational points. This can be seen from Fig. 20 for the case when the rated load is applied. The error of the loss calculated using the improved analytical model may fluctuate differently at stator frequencies other than 50 Hz. This is mostly due to the narrow range of frequencies used for the data fitting of the SLL and the loss caused by the skin effect in rotor bars, as well as to the accuracy of these fits. Nonetheless, when applying rated frequency and voltage to the improved model, the total loss error is below 5 % in any loading condition. In the case of the rated operational point, the total loss error is only 0.57 %, which is a significant improvement comparing to almost 20 % total loss error

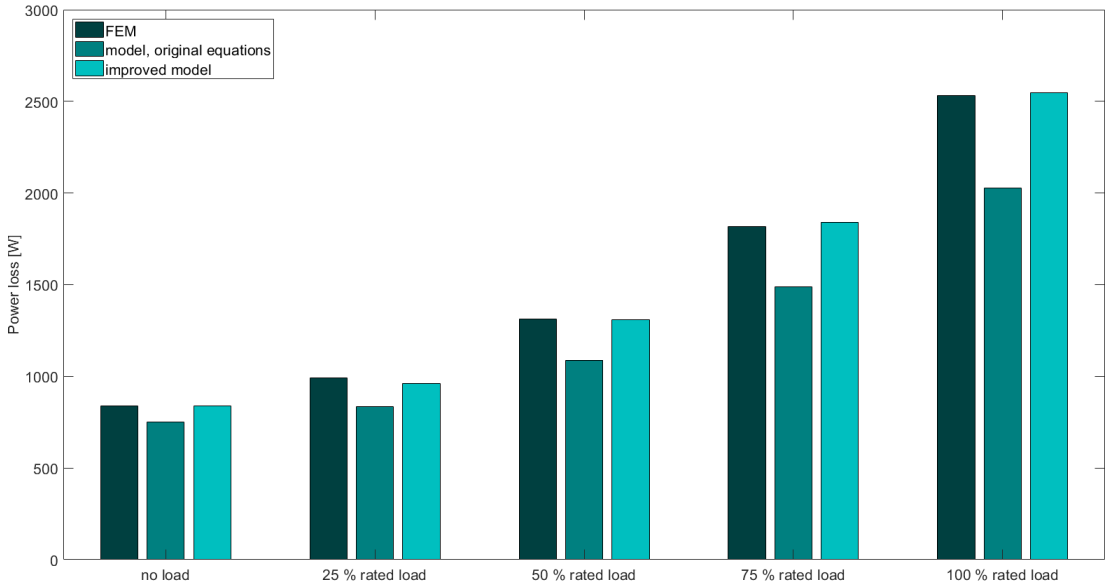

Figure 21: Total EM loss of the 45 kW motor at the varying load

calculated using the original analytical model.

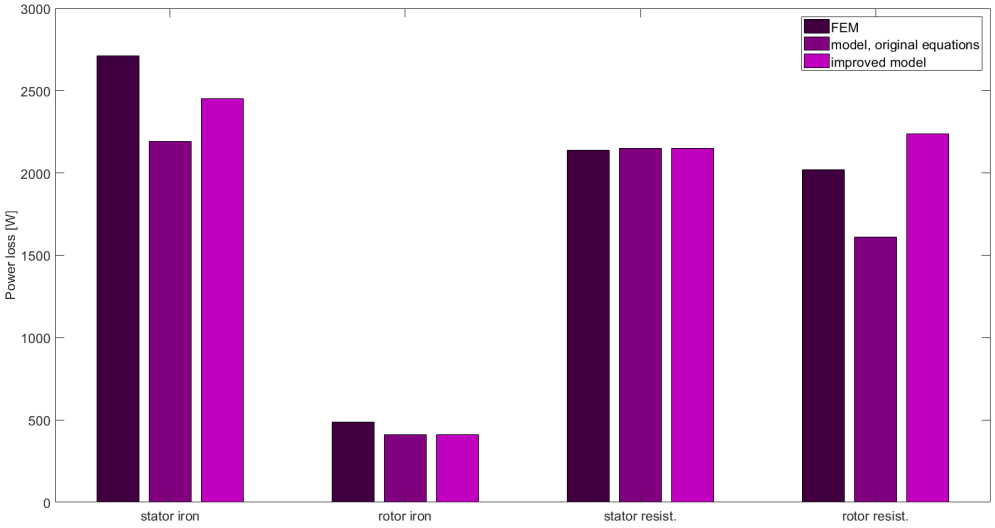

Figure 22: 250 kW motor loss components at the rated load

Only final results are presented for the 250 kW motor. All the parameters of the proposed model of the 250 kW motor are given in Table 4. Fig. 22 shows the comparison of the "original" and the improved (proposed) analytical model of the 250 kW motor to the FEM loss computations, while Fig. 23 shows the total electromagnetic loss of the 45 kW motor at different loading conditions. It can be seen that the loss results calculated using the improved model are closer to the FEM

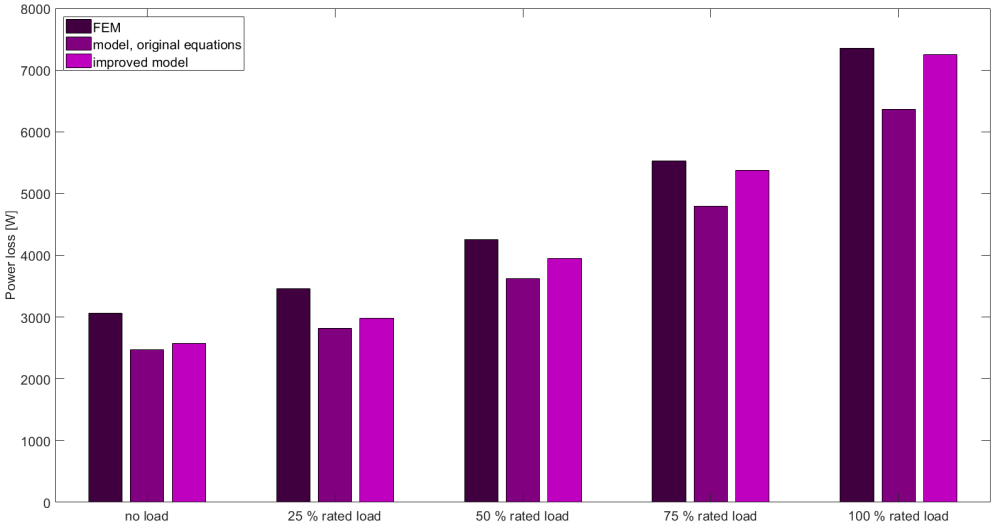

Figure 23: Total EM loss of the 250 kW motor at the varying load

computations for each loss component. In addition, the total loss calculated using the improved model are closer to the FEM computations, in comparison to the original model. However, the error of the improved loss model is higher in the case of the 250 kW motor compared to the 45 kW motor. This is mostly due to the parameter fitting not being as close in the case of the 250 kW motor as they were for the 45 kW motor. The error almost linearly decreases from 16 % in the no load condition to only 1.5 % at the rated load.

Nonetheless, simulated stator currents and torques of both the 45 kW and the 250 kW motors are matching very closely to the values of the same variables computed by FEM. For the 45 kW motor, the simulated stator current at the rated point equals 81.81 A, which differs only slightly from 81.94 A computed by FEM. Additionally, simulated torque amounts to 290 Nm, which is almost identical to the value computed by FEM: 289.98 Nm. In the case of the 250 kW motor, simulated rated stator current reaches 353.84 A, while this current according to FEM is 351.76 A. In addition, simulated torque reaches 1603 Nm compared to 1603.21 Nm from FEM.

Table 4: Equation parameters for the 250 kW motor

Parameter	**Value**
k_{s}	551.72
n_{s}	2.02
$R_{\mathrm{Ft,s}}$	296.47
k_{R}	4.03
n_{R}	1.03
$R_{\mathrm{Ft,R}}$	579.00
k_1	0.0014
n_{s1}	1.65
n_{s2}	1.84
k_2	0.0001
n_{R1}	0.86
n_{R2}	1.72
α	0.025
a	7.09
β	0.047
b	9.48

5 Conclusions and future work

This thesis has successfully designed an improved induction motor model. The induction machine model represented by a Γ equivalent circuit augmented with an iron loss model was proposed in [5] and used as the basis for the improved model. The electromagnetic loss calculation has been improved by accounting for the iron loss due to loading and by including the loss due to the skin effect in the rotor bars. Finite element analysis was performed to identify parameters of the improved model, as well as to validate the results. The proposed model has been implemented in the MATLAB Simulink environment and can be integrated with an electric drive simulation.

Testing of the Simulink model was performed using a simple rotor flux oriented vector control with a sinusoidal input in order to make the results comparable to the results of FEM. All the FEM computations were done using the 2D time-stepping analysis in the FC-SMEK software. Parameter identification was accomplished using *lsqnonlin*, the nonlinear least squares data fitting method offered by MATLAB.

The induction motor model proposed in [5] has been augmented by only one nonlinear element, which enabled the calculation of the stator no load iron loss and the rotor iron loss separately. This allows for a more in-depth analysis of the origin of the machine losses. Moreover, a similar approach was used as in [5] to separate eddy-current from hysteresis loss in both the stator and the rotor iron. In addition to that, the stator iron loss due to loading of the machine has been modelled as well. This improvement has reduced the error of the stator iron loss prediction in the rated point of operation of the 45 kW motor by over 20 % in comparison with the model based on the no load iron loss. Furthermore, the proposed model has incorporated the calculation of the eddy-current loss in the rotor bars, which has improved the prediction of the total resistive loss in the rotor by over 23 % in the rated point. In addition to the two nonlinear resistances, two inductances with simple nonlinear functions have replaced the constant inductances of a standard Γ-model. By accounting for the saturation of the magnetising inductance as a function of the main flux and the saturation of the leakage inductance as a function of the rotor current, the magnetic saturation of the machine has been modelled. If a certain application requires a mutual saturation model, these simple inductance formulas can be enhanced by including the dependency of the magnetising inductance on the rotor current and the dependency of the leakage inductance on the main flux. Such equations were proposed in [3] and [5]. All the implemented improvements have decreased the total electromagnetic loss prediction error by over 10 % in the no load operation and over 19 % in the rated point for the 45 kW motor.

Due to simplicity of the proposed model, it is easy and straightforward to implement it in the MATLAB Simulink environment, in which the model can run in real time. Hence, it is possible to integrate the model with an electric drive simulation, which can be used in a variety of applications. However, the integration was not in the scope of this thesis, so it will need to be performed in the future. Furthermore, the losses are calculated in real time as well, as opposed to models such as FEM-based ones, in which loss computation is done in post-processing. This allows for the usage

of the proposed model even in the applications in which online loss monitoring is required. In order to use the Simulink model for a chosen induction machine, it is necessary to first perform a series of FEM simulations in order to collect data for parameter identification. Once the parameters are determined for the particular motor, the model can be run in real time.

Since the model was based on the computations performed with the sinusoidal input voltage, it is not suitable for prediction of the behaviour of the power losses resulting from the presence of the higher harmonics. A proposal for future work is thus to study the effects of the non-fundamental harmonics resulting from the inverter operation on the losses and include it in the motor model. This will improve the prediction of the efficiency of the whole system.

References

[1] G. Slemon, “Modelling of induction machines for electric drives,” *IEEE Transactions on Industry Applications*, vol. 25, no. 6, pp. 1126–1131, 1989.

[2] M. Sokola, E. Levi, G. Jamieson, and D. Williams, “Representation and compensation of iron loss in rotor flux oriented induction machines,” *Proceedings of International Conference on Power Electronics, Drives and Energy Systems for Industrial Growth*, 1996.

[3] T. Tuovinen, M. Hinkkanen, and J. Luomi, “Modeling of Mutual Saturation in Induction Machines,” *2008 IEEE Industry Applications Society Annual Meeting*, 2008.

[4] L. Harnefors, M. Hinkkanen, O. Wallmark, A. Gomez Yepes, *Control of Voltage-Source Converters and Variable-Speed Drives*, unpublished.

[5] M. Ranta, M. Hinkkanen, E. Dlala, A.-K. Repo, and J. Luomi, “Inclusion of hysteresis and eddy current losses in dynamic induction machine models,” *2009 IEEE International Electric Machines and Drives Conference*, 2009.

[6] M. Elmahfoud, B. Bossoufi, M. Taoussi, N. E. Ouanjli, and A. Derouich, “Rotor Field Oriented Control of Doubly Fed Induction Motor,” *2019 5th International Conference on Optimization and Applications (ICOA)*, 2019.

[7] A. Faizan, "Three Phase Induction Motor Construction", *Electrical Academia*, n.d. [Online]. Available: http://electricalacademia.com/induction-motor/three-phase-induction-motor-construction/. [Accessed: November 11, 2019].

[8] Y. Kawase, T. Yamaguchi, Z. Tu, N. Toida, N. Minoshima, and K. Hashimoto, “Effects of Skew Angle of Rotor in Squirrel-Cage Induction Motor on Torque and Loss Characteristics,” *IEEE Transactions on Magnetics*, vol. 45, no. 3, pp. 1700–1703, 2009.

[9] J. Pyrhönen, T. Jokinen, and V. Hrabovcova, *Design of rotating electrical machines*. Chichester, U.K.: J. Wiley Sons, 2014.

[10] "Design of Induction Motors", *BrainKart*, n.d. [Online]. Available: https://www.brainkart.com/article/Design-of-Induction-Motors_12303/. [Accessed: November 11, 2019].

[11] N. Watanabe, I. Hirotsuka, H. Sugimoto, and M. Nakamura, “Trial Fixed Outer Rotor Three-Phase Squirrel-Cage Induction Motor and its Basic Characteristics,” *2018 21st International Conference on Electrical Machines and Systems (ICEMS)*, 2018.

[12] A. Chiba and J. Asama, “Influence of Rotor Skew in Induction Type Bearingless Motor,” *IEEE Transactions on Magnetics*, vol. 48, no. 11, pp. 4646–4649, 2012.

[13] G. Garcia, J. Luis, R. Stephan, and E. Watanabe, “An efficient controller for an adjustable speed induction motor drive,” *IEEE Transactions on Industrial Electronics*, vol. 41, no. 5, pp. 533–539, 1994.

[14] T. Javied, T. Rackow, R. Stankalla, C. Sterk, and J. Franke, “A Study on Electric Energy Consumption of Manufacturing Companies in the German Industry with the Focus on Electric Drives,” *Procedia CIRP*, vol. 41, pp. 318–322, 2016.

[15] https://www.eia.gov/energyexplained/electricity/use-of-electricity.php

[16] A. Boglietti, A. Cavagnino, M. Lazzari, and M. Pastorelli, “International Standards for the Induction Motor Efficiency Evaluation: A Critical Analysis of the Stray-Load Loss Determination,” *IEEE Transactions on Industry Applications*, vol. 40, no. 5, pp. 1294–1301, 2004.

[17] H. Karkkainen, L. Aarniovuori, M. Niemela, J. Pyrhonen, J. Kolehmainen, T. Kansakangas, and J. Ikaheimo, “Direct-On-Line Synchronous Reluctance Motor Efficiency Verification with Calorimetric Measurements,” *2018 XIII International Conference on Electrical Machines (ICEM)*, 2018.

[18] B. Silwal, "Power Balance in the Finite Element Analysis of Electrical Machines", Ph.D. dissertation, Dept. of Elec. End. and Automation, Aalto Univ., Espoo, Finland, 2017. Accessed on: Dec 16, 2019 [Online]. Available: https://aaltodoc.aalto.fi/handle/123456789/26234

[19] M. Ranta, "Dynamic induction machine models including magnetic saturation and iron losses", Ph.D. dissertation, Dpt. of Elec. Eng., Aalto Univ., Espoo, Finland, 2013.

[20] G. Bertotti, “General properties of power losses in soft ferromagnetic materials,” *IEEE Transactions on Magnetics*, vol. 24, no. 1, pp. 621–630, 1988.

[21] "Magnetic Properties of Engineering Materials", *Electrical 4 U*, Nov. 3, 2019 [Online]. Available: https://www.electrical4u.com/magnetic-properties-of-engineering-materials/. [Accessed: November 25, 2019].

[22] C. P. Steinmetz, “On the Law of Hysteresis,” *Transactions of the American Institute of Electrical Engineers*, vol. IX, no. 1, pp. 1–64, 1892.

[23] H. Jordan, “Die ferromagnetischen Konstanten für schwache Wechselfelder”, *Elektr. Nach. Techn.*, vol. 1, p. 8, 1924.

[24] A. Belahcen, P. Rasilo, and A. Arkkio, “Segregation of Iron Losses From Rotational Field Measurements and Application to Electrical Machine,” *IEEE Transactions on Magnetics*, vol. 50, no. 2, pp. 893–896, 2014.

[25] G. Bertotti, “Physical interpretation of eddy current losses in ferromagnetic materials. I. Theoretical considerations,” *Journal of Applied Physics*, vol. 57, no. 6, pp. 2110–2117, 1985.

[26] M. Sokola, E. Levi, A. Boglietti, and M. Pastorelli, “Detuned operation of rotor flux oriented induction machines in the field-weakening region due to iron loss,” *IEE Colloquium on Vector Control and Direct Torque Control of Induction Motors*, 1995.

[27] M. Sokola and E. Levi, “Combined impact of iron loss and main flux saturation on operation of vector controlled induction machines,” *6th International Conference on Power Electronics and Variable Speed Drives*, 1996.

[28] E. Levi, M. Sokola, A. Boglietti, and M. Pastorelli, “Iron loss in rotor-flux-oriented induction machines: identification, assessment of detuning, and compensation,” *IEEE Transactions on Power Electronics*, vol. 11, no. 5, pp. 698–709, 1996.

[29] L. Chua and K. Stromsmoe, “Lumped-circuit models for nonlinear inductors exhibiting hysteresis loops,” *IEEE Transactions on Circuit Theory*, vol. 17, no. 4, pp. 564–574, 1970.

[30] A. Arkkio, "Analysis of induction motors based on the numerical solution of the magnetic field and circuit equations", Ph.D. dissertation, Department of Electrical and Communications Eng., Helsinki University of Techonology, Espoo, Finland, 1987.

[31] L. Aarniovuori, P. Lindh, H. Karkkainen, M. Niemela, J. Pyrhonen, and W. Cao, “Analytical Evaluation of High-Efficiency Induction Motor Losses”, *2019 IEEE International Electric Machines Drives Conference (IEMDC)*, 2019.

[32] J. Lammeraner, M. Stafl, and G. A. Toombs, *Eddy currents*. London: Iliffe Books, 1966.

[33] M. J. Islam, H. V. Khang, A.-K. Repo, and A. Arkkio, “Eddy-Current Loss and Temperature Rise in the Form-Wound Stator Winding of an Inverter-Fed Cage Induction Motor,” *IEEE Transactions on Magnetics*, vol. 46, no. 8, pp. 3413–3416, 2010.

[34] L. Aarniovuori, M. Niemela, J. Pyrhonen, W. Cao, and E. B. Agamloh, “Loss Components and Performance of Modern Induction Motors,” *2018 XIII International Conference on Electrical Machines (ICEM)*, 2018.

[35] B. Chalmers and A. Williamson, “Stray losses in squirrel-cage induction motors. Validity of the reverse-rotation test method,” *Proceedings of the Institution of Electrical Engineers*, vol. 110, no. 10, p. 1773, 1963.

[36] A. A. Jimoh, R. D. Findlay, and M. Poloujadoff, “Stray Losses in Induction Machines: Part II, Calculation and Reduction,” *IEEE Power Engineering Review*, vol. PER-5, no. 6, pp. 59–60, 1985.

[37] R. S. Kanchan and R. R. Moghaddam, "Experimental validation of a novel core-loss model including additional harmonic losses for online energy efficient control of induction motors," *2017 IEEE International Electric Machines and Drives Conference (IEMDC)*, 2017.

[38] K. Dabala, "Analysis of mechanical losses in three-phase squirrel-cage induction motors," *ICEMS2001. Proceedings of the Fifth International Conference on Electrical Machines and Systems (IEEE Cat. No.01EX501)*, 2001.

[39] C. Gerada, K. J. Bradley, M. Sumner, and P. Sewell, "Evaluation and Modeling of Cross Saturation Due to Leakage Flux in Vector-Controlled Induction Machines," *IEEE Transactions on Industry Applications*, vol. 43, no. 3, pp. 694–702, 2007.

[40] M. Hinkkanen, A.-K. Repo, and J. Luomi, "Influence of magnetic saturation on induction motor model selection," in *Proc. ICEM'06*, Chania, Greece, Sept. 2006.

[41] R. Lorenz and D. Novotny, "Saturation effects in field-oriented induction machines," *IEEE Transactions on Industry Applications*, vol. 26, no. 2, pp. 283–289, 1990.

[42] C. Sullivan and S. Sanders, "Models for induction machines with magnetic saturation of the main flux path," *IEEE Transactions on Industry Applications*, vol. 31, no. 4, pp. 907–917, 1995.

[43] H. C. J. de Jong, "Saturation in electrical machines," in *Proc. ICEM'80*, vol. 3, Athens, Greece, Sept. 1980, pp. 1545–1552.

[44] Z. Qu, M. Ranta, M. Hinkkanen, and J. Luomi, "Loss-minimizing flux level control of induction motor drives," *2011 IEEE International Electric Machines Drives Conference (IEMDC)*, 2011.

[45] M. Ranta and M. Hinkkanen, "Online identification of parameters defining the saturation characteristics of induction machines," *2012 XXth International Conference on Electrical Machines*, 2012.

[46] J. C. Maxwell, *A treatise on Electricity and Magnetism.* Oxf., 1873.

[47] P. Monk, *Finite element methods for Maxwell's equations.* Oxford: Clarendon Press, 2008.

[48] J. Luomi, *Finite element methods for electrical machines*, Göteborg, 1993.

[49] A. Lehikoinen, Class Lecture, Topic: "Lecture 4", ELEC-E8411, School of Electrical Engineering, Aalto University, Espoo, Mar. 2018.

[50] Lecture notes, Topic: "Nonlinear Least Squares Data Fitting", PHYS 159, Faculty of Science, University of British Columbia, Vancouver, BC, Canada. Available at: http://math.gmu.edu/ igriva/book/Appendix%20D.pdf

[51] "lsqnonlin", *MathWorks*, n.d. [Online]. Available: https://se.mathworks.com/help/optim/ug/lsqnonlin.html. [Accessed: November 17, 2019]

[52] L. Aarniovuori, P. Rasilo, M. Niemela, and J. J. Pyrhonen, "Analysis of 37-kW Converter-Fed Induction Motor Losses," *IEEE Transactions on Industrial Electronics*, vol. 63, no. 9, pp. 5357–5365, 2016.

[53] E. Dlala, O. Bottauscio, M. Chiampi, M. Zucca, A. Belahcen, and A. Arkkio, "Numerical Investigation of the Effects of Loading and Slot Harmonics on the Core Losses of Induction Machines," *IEEE Transactions on Magnetics*, vol. 48, no. 2, pp. 1063–1066, 2012.